

國立臺灣大學電機資訊學院生醫電子與資訊學研究所



碩士論文

Graduate Institute of Biomedical Electronics and Bioinformatics

College of Electrical Engineering and Computer Science

National Taiwan University

Master's Thesis

整合氣液微流道與表面增強拉曼光譜基板進行吸附性代謝物

分離之細菌鑑別

Integration of Air-liquid Microfluidics and SERS Substrate for

Bacteria Identification Based on Adsorptive Separation

顧啟耀

Chi-Yao Ku

指導教授：黃念祖 博士

Advisor: Nien-Tsu Huang, Ph.D.

中華民國 2024 年 6 月

June, 2024

國立臺灣大學碩士學位論文
口試委員會審定書

MASTER'S THESIS ACCEPTANCE CERTIFICATE
NATIONAL TAIWAN UNIVERSITY

整合氣液微流道與表面增強拉曼光譜基板進行吸附性代謝物

分離之細菌鑑別

Integration of Air-liquid Microfluidics and SERS Substrate for
Bacteria Identification Based on Adsorptive Separation

本論文係 顧啟耀 (R11945007) 在國立臺灣大學電機資訊學院生醫電子與資訊學研究所完成之碩士學位論文，於民國 113 年 06 月 13 日承下列考試委員審查通過及口試及格，特此證明。

The undersigned, appointed by the Graduate Institute of Biomedical Electronics and Bioinformatics, College of Electrical Engineering and Computer Science, National Taiwan University on 13, June 2024 have examined a Master's thesis entitled above presented by Chi-Yao, Ku (R11945007) candidate and hereby certify that it is worthy of acceptance.

口試委員 Oral examination committee:

黃念祖

蔣新仰

王俊凱

(指導教授 Advisor)

王石麟
林致廷

所長 Director: _____

誌謝



能完成這份碩士論文以及完成我的研究，依靠了蠻多人的幫助。首先，要感謝大涵學長以及明雋學長，在碩一時對剛進來的我細心教導，讓我認識了實驗室的各種資源以及機台的使用。接下來要感謝赫文學長以及淮原學長，耐心的教導我拉曼機台以及細菌培養的基礎知識以及技巧，感謝他們不間斷的提供底板材料支援我的研究。感謝王鈞、彥安與子瑜，在我上課時遇到困難時給予幫助。也要感謝宣融、冠均及彥程，一起互相扶持面對未來即將面對的困境。我要感謝實驗室的每一位成員，在我實驗面臨困難時給予我方向，以及在會議中提出對報告的建議，使我在不斷的報告過程中學習。接下來要感謝在月會中提供建議以及問題的老師，讓我對自己研究的方向以及脈絡有足夠的認知，學習建構自己的研究邏輯。我要特別感謝我的指導教授黃念祖老師，在每一次的個別會議中，對我的報告進行建議以及指導，提供面對困難時可以解決問題的方向，並督促自己的研究進度。總而言之，要感謝的事情太多了，謝謝大家。

顧啟耀

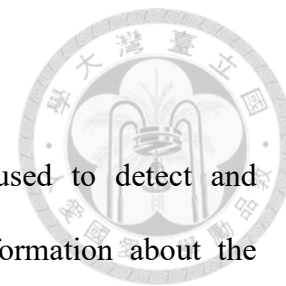
2024年6月

摘要



表面增強拉曼光譜(SERS)在這近 50 年間常被應用於細菌鑑別的檢測，這項技術在這個領域提供了各種生物分子組成資訊，像是腺嘌呤、次黃嘌呤、腺嘧啶與其他嘌呤的代謝產物，但相同或是類似結構的分子光譜會重疊在一起或者被親和力較大的分子所覆蓋，所以我們提供了一種吸附性分離的晶片，結合了表面增強拉曼光譜的量測技術與氣液微流道分離複雜溶液中的多重分子，當使用壓力幫浦提供穩定的脈衝流速的同時，液珠會流進微流道中的液珠停留區中等待特定的時間和表面增強拉曼光譜基板相互作用進行吸附性分離，由於親和力不同，含有多個分子的溶液可以依序被分離到不同的井中並使用表面增強拉曼光譜檢測。在初步結果中，我們設計了不同的流道寬度設計，發現 0.4 mm 的流道寬度設計能減少溶液殘留，也優化 3 分鐘的反應時間以及 300 μm 的流道寬度能觀察 10^{-5} 到 10^{-6} M 濃度的腺嘌呤衰減曲線。將腺嘌呤以及腺嘧啶做不同比例混和之後，可觀察到腺嘧啶的訊號在一開始被腺嘌呤的訊號所屏蔽，但在使用微流道系統之後，腺嘧啶的訊號會被顯現出來，驗證了吸附性分離的能力。在主成分分析之中，與傳統方法做相比，不同細菌上清液可以被清晰的分群，展現它細菌鑑別的能力。因此這個微流道平台可用於鑑別不同菌種的細菌，提供對含有多重分析物溶液的見解，突破了傳統表面增強拉曼光譜檢測的限制。

Abstract



Surface-enhanced Raman Spectroscopy (SERS) has been used to detect and recognize bacteria for five decades. This technique supplies information about the components of different biomolecules, such as adenine, hypoxanthine, uracil, and other purine derivatives. However, the SERS signals of compounds with similar structures would overlap together or be surpassed by the one with strong affinity. We proposed an adsorptive separation method that combines the SERS technique with air-liquid microfluidics to separate multiple molecules in complex solutions. Adsorptive separation occurred when the droplet flowed into different wells in the air-liquid microfluidics, while the pressure pump supplied the stable pressure and impulse wave of flow rate. Thus, the solution containing multiple molecules could sequentially be separated into different wells due to the different affinity. In the results, we designed channels with different widths and found that a channel width of 0.4 mm can save the volume loss. We also discovered that a reaction time of 3 minutes and a channel width of 300 μm allowed us to observe the attenuation curve of adenine concentrations from 10^{-5} to 10^{-6} M. After mixing adenine and uracil in different proportions, we observed that the signal of uracil was initially masked by the signal of adenine. However, using our microfluidic system, the signal of uracil could be revealed, confirming the capability of adsorptive separation. In the principal component analysis (PCA), different kinds of bacterial supernatants could be clustered clearly compared to the traditional method, showing the ability of bacteria identification. Therefore, this microfluidic platform helps us to distinguish the different species of bacteria, and it also can provide insights into the multiplex analytes contained solution, breaking the limitation of traditional SERS detection.

Contents



口試委員會審定書	#
誌謝	i
摘要	ii
Abstract.....	iii
Contents.....	iv
List of Figures.....	vi
List of Tables	xi
Chapter 1 Introduction.....	1
1.1 Research Background	1
1.2 Literature Review	3
1.2.1 SERS in Microfluidic for Bacteria Identification	3
1.2.2 The Arts of Air-liquid Microfluidics	8
1.2.3 Adsorptive Separation and Bacterial Supernatant.....	15
1.3 Research Motivation.....	18
Chapter 2 Theory	19
2.1 Raman Scattering.....	19
2.2 SERS Theory	20
2.3 The Behavior of the Air-Liquid Interface	22
Chapter 3 Materials and Methods.....	24
3.1 Reagents.....	24
3.2 Bacteria Incubation and Supernatant Extraction	24
3.3 Device Design and Fabrication.....	25
3.3.1 Mold Fabrication.....	27

3.3.2	PDMS Chip Fabrication.....	27
3.4	Combination of SERS Substrate and PDMS Chip.....	28
3.5	Pressure Pumping System.....	29
3.6	The Optical and Fluorescent Microscope.....	31
3.7	SERS Measurement.....	31
3.7.1	SERS Substrate.....	31
3.7.2	Raman Microscope Setup.....	32
3.7.3	Data Processing.....	33
3.8	System Setup.....	33
Chapter 4	Results and Discussion.....	35
4.1	Mold Fabrication.....	35
4.2	Burst Pressure Experiment in Microfluidic Device.....	35
4.3	Optimization of Microfluidic Device Geometry.....	36
4.4	Adsorption of Single Analyte.....	40
4.4.1	Adsorption Time Evaluation.....	40
4.4.2	Channel Height Evaluation.....	42
4.4.3	Adsorption with Different Compounds.....	45
4.5	Competitive Adsorption of Two Analytes.....	48
4.6	Bacteria Identification by Microfluidic Device.....	50
4.7	Principal Component Analysis (PCA).....	52
4.8	Machine Learning Method of Supporting Vector Machine (SVM).....	53
Chapter 5	Conclusions.....	55
Chapter 6	Future Work.....	56
	REFERENCE.....	58

List of Figures

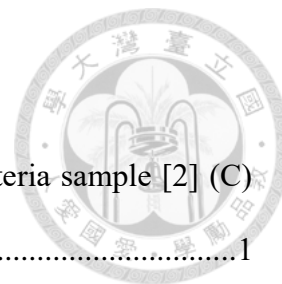


Figure 1 The application of SERS on (A) urine sample [1] (B) bacteria sample [2] (C) fruit. [4].....	1
Figure 2 (A) A droplet microfluidic combines with magnetic beads for SERS hotspot generation. [5] (B) A microfluidic device combines with DEP for protein capture. [6] (C) The schematic of SERS detection in a microfluidic system. [7] (D) A microfluidic device that combines the FFE separation technique for nanoparticle aggregation. [8].....	3
Figure 3 (A) A microfluidic device that uses electrokinetic force to concentrate nanoparticles for SERS detection. [10] (B) A droplet microfluidic that mixes KCl solution and test solution for nanoparticle aggregation and SERS detection. [11] (C) A microfluidic device for bacteria washing and SERS detection at the same time. [13] (D) A microfluidic device for antibiotic concentration gradient generation. [15].....	5
Figure 4 (A) The SERS spectrum of bacteria in the Genus of <i>Mycobacterium</i> . [16] (B) The SERS spectrum of <i>E. coli</i> DH5 α WT and kanamycin-resistant strain. [14]	6
Figure 5 (A) The system setup of the T-junction microfluidics and the high-speed camera. (B) The image of mixing results and homogeneity factor before and after mixing. [18]	8
Figure 6 (A) The image of the tree-like airway microfluidics. (B) The plug velocity in each generation number. The dashed line is calculated by the previous report, while the solid line is the average velocity. (C) The resistance in each generation number. (D) The plot of the total flow rate and the generation	

number. [19].....	9
Figure 7 (A) The design of the disposable flow cytometry microfluidic system. (B) The image of the flow with the flow rate of 6 and 5 mL/hr under the constant vacuum pressure. [20].....	10
Figure 8 (A) The relationship between Weber number and the plug formation. (B) The relationship between Laplace pressure and insert pressure. [21]	11
Figure 9 (A) The process of first-come-first-store microfluidics. (B) The burst pressure of different kinds of channel design. [22]	12
Figure 10 (A) The schematic of the microfluidic-based multicolor display. (B) The pattern of pressure supplied by the vacuum pump and monitored by the PC. (C) The volume loss evaluation under the different kinds of design and channel width and height. [23]	13
Figure 11 The illustration of adsorptive separation. [25]	15
Figure 12 (A) The purine metabolic pathways of different bacteria. [9] (B) The SERS spectrum of different bacterial supernatants. [9]	16
Figure 13 The DFT simulation of adenine bonding with silver surface. [26]	16
Figure 14 (A) The uracil binds with the silver surface at different pH values. [28] (B) The thymine binds with the silver surface in different forms. [27] (C) The electrochemical reaction of serotonin, epinephrine, dopamine, norepinephrine, and catechol with different running times. [29].....	17
Figure 15 The principle of Raman scattering. [30]	19
Figure 16 The electromagnetic enhancement and chemical enhancement in the SERS mechanism. [32]	22
Figure 17 The relationship between Weber number and air-liquid flow. [21].....	23
Figure 18 The relationship between the contact angle and the gap between two solid	

surfaces. [33].....	23
Figure 19 The design of the microfluidic chip with a channel width of (A) 0.5 mm (B) 0.4 mm (C) 0.3 mm. (D) The final design of the microfluidic chip used for the SERS detection.	26
Figure 20 The CNC machine of (A) Roland MDX-50 (B) Roland EGX-400.	27
Figure 21 The process of chip fabrication.	29
Figure 22 (A) The image of the pressure pump. (OB1) (B) The flow rate and pressure reported from OB1 and the flow sensor. (C) The schematic of the pressure pump setup.....	30
Figure 23 (A) The SEM image of the SERS substrate (scale bar = 200 nm). [13] (B) The SERS spectrum and Raman spectrum of Rhodamine 6G solution in a concentration of 10^{-6} M and 10^{-2} M, respectively, and $EF = 4.17E4$	32
Figure 24 The Raman microscope. [36]	33
Figure 25 (A) System schematic of air-liquid microfluidic and Raman microscope. (B) The real image of the system schematic.	34
Figure 26 (A) The PMMA mold was fabricated by Roland MDX-50. (B) The PMMA mold was fabricated by Roland EGX-400.....	35
Figure 27 The fluorescent image of the microfluidic channel after the droplet moved. .	37
Figure 28 The air-liquid microfluidics performance under the fluorescent microscope.	38
Figure 29 The setup of the pressure pumping system and fluorescent microscope.	39
Figure 30 (A) Schematic of SERS detection by pipette. The SERS spectrum of 10^{-5} M adenine in different positions with adsorption time of (B) 1 min (C) 3 min (D) 5 min. (E) The attenuation of the SERS signal at 733 cm^{-1} under different adsorption times (1, 3, and 5 minutes). (F) Schematic of SERS detection by the pumping system. SERS spectrum of 10^{-5} M adenine in different wells with	

adsorption time of (G) 1 min (H) 3 min (I) 5 min. (J) The attenuation of the SERS signal at 733 cm^{-1} under different adsorption times in the pumping system (1, 3, and 5 minutes).42

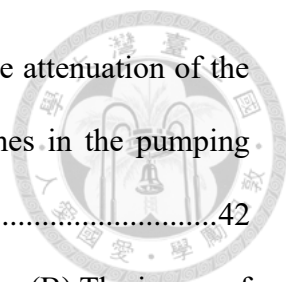


Figure 31 (A) The combination of PDMS channel and SERS substrate. (B) The image of the microfluidic chip in the chip mailer and vacuumed by the package machine. (C) The microfluidic chip invert is placed on the mold of the motorized stage. (D) The Raman microscope and our microfluidic chip. (E) The microfluidic chip is connected to a pressure pump under the Raman microscope.42

Figure 32 (A) Schematic of SERS detection by the pumping system with the adsorption time of 3 minutes. The SERS spectrum of (B) 10^{-5} M (C) $5 \times 10^{-6}\text{ M}$ (D) 10^{-6} M adenine in different wells with a channel height of $600\text{ }\mu\text{m}$. (E) The attenuation curve at 733 cm^{-1} with a channel height of $600\text{ }\mu\text{m}$. The SERS spectrum of (F) 10^{-5} M (G) $5 \times 10^{-6}\text{ M}$ (H) 10^{-6} M adenine in different wells with a channel height of $300\text{ }\mu\text{m}$. (I) The attenuation curve at 733 cm^{-1} with a channel height of $300\text{ }\mu\text{m}$. The SERS spectrum of (J) 10^{-5} M (K) $5 \times 10^{-6}\text{ M}$ (L) 10^{-6} M adenine in different wells with a channel height of $150\text{ }\mu\text{m}$. (M) The attenuation curve at 733 cm^{-1} with a channel height of $150\text{ }\mu\text{m}$44

Figure 33 The dynamic range of the (A) guanine (B) hypoxanthine (C) adenine (D) cytosine (E) thymine (F) uracil in the SERS detection method.46

Figure 34 The SERS spectrum of (A) 10^{-4} M guanine (B) 10^{-5} M hypoxanthine (C) 10^{-5} M adenine (G) 10^{-4} M cytosine (H) 10^{-4} M thymine (I) 10^{-5} M uracil in our microfluidic system (3 minutes adsorption time and $300\text{ }\mu\text{m}$ channel height). The attenuation of the SERS signal at (D) 660 cm^{-1} (E) 740 cm^{-1} (F) 733 cm^{-1} (J) 796 cm^{-1} (K) 780 cm^{-1} (L) 800 cm^{-1}47

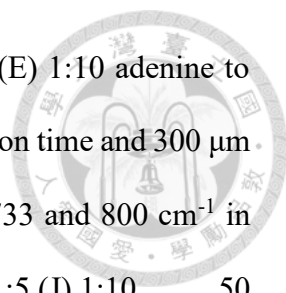


Figure 35 The SERS spectrum of (A) 10:1 (B) 5:1 (C) 1:1 (D) 1:5 (E) 1:10 adenine to uracil ratio in our microfluidic system (3 minutes adsorption time and 300 μm channel height). The attenuation of the SERS signal at 733 and 800 cm^{-1} in the adenine to uracil ratio of (F) 10:1 (G) 5:1 (H) 1:1 (I) 1:5 (J) 1:10.....50

Figure 36 The SERS spectrum of bacterial supernatant of (A) *E. coli* BW25113 (B) *E. coli* BL21 (C) *E. coli* DH5 α WT (D) *E. coli* DH5 α Amp^r (E) *B. subtilis* ATCC 6633 in our microfluidic system (3 minutes adsorption time and 300 μm channel height). The attenuation of SERS signal at 725 and 800 cm^{-1} in the bacterial supernatant of (F) *E. coli* BW25113 (G) *E. coli* BL21 (H) *E. coli* DH5 α WT (I) *E. coli* DH5 α Amp^r (J) *B. subtilis* ATCC 6633.52

Figure 37 (A) The PCA of the only well 1 data in each sample (N=9). (B) The PCA of combining well 1 to well 8 data in each sample (N=9).....53

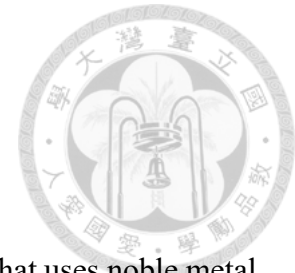
Figure 38 (A) The confusion matrix of SVM with only well 1 data in each sample (N=27). (B) The confusion matrix of SVM with combining well 1 to well 8 data in each sample (N=27).....54

List of Tables



Table 1 List of several bacteria identification research by SERS and microfluidic platform	7
Table 2 List of several air-liquid microfluidic research.....	14
Table 3 The parameters of the pressure pump.	30
Table 4 The volume loss analysis of different channel widths.....	37
Table 5 The surface area analysis at different wells.	39

Chapter 1 Introduction



1.1 Research Background

Surface-enhanced Raman Spectroscopy (SERS) is a technique that uses noble metal nanoparticles to enhance the electromagnetic field between the nanoparticles, thus enhancing the signal of Raman. It reflects the vibrational fingerprint of molecules at different wavelength shifts. There are different methods to generate SERS hotspots, including colloid and non-colloid methods. Nowadays, SERS has already been applied to the detection of biomolecules in urine, bacteria, blood, drugs, and agricultural pesticides. For example, Jung Bin Phyto et al. used the silver nanowire to detect the urine from patients with pancreatic cancer and prostate cancer (Figure 1A). [1] Wei Wang et al. used SERS tap to detect the volatile compounds and nonvolatile compounds that *P. syringae* secrete (Figure 1B). [2] Abed Haddad et al. used the SERS technique to detect fentanyl, a drug that is used as a treatment for cancer and chronic pain. [3] Lili He et al. used the SERS technique to detect the thiabendazole on apples (Figure 1C). [4]

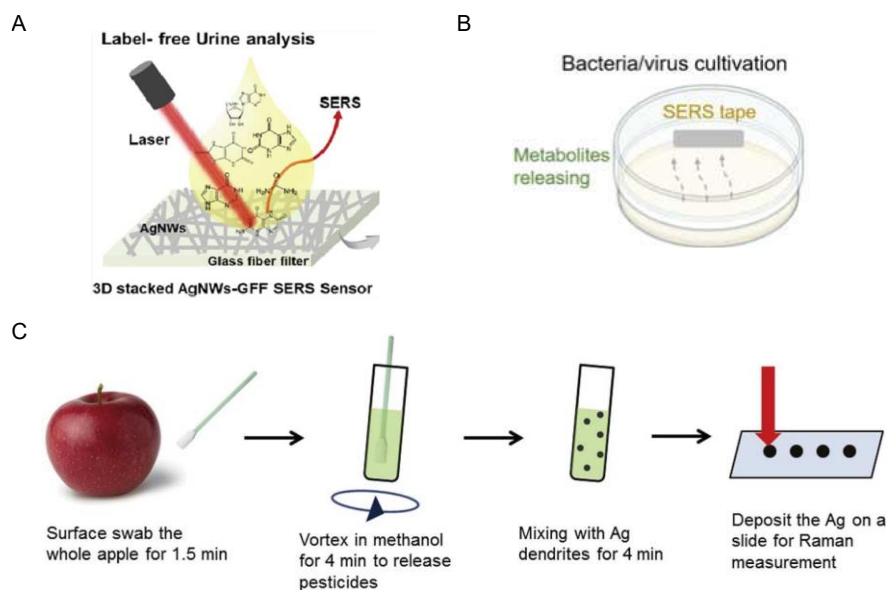
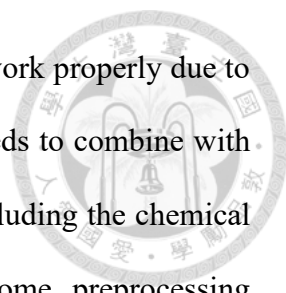


Figure 1 The application of SERS on (A) urine sample [1] (B) bacteria sample [2] (C) fruit. [4]



Without sample preprocessing, the SERS technique could not work properly due to the blocking of other impurities. Therefore, the SERS technique needs to combine with the microfluidic system to perform precise biomolecule sensing, including the chemical inert and transparency of polydimethylsiloxane (PDMS) and some preprocessing techniques provided by microfluidics itself. For example, Namhyun Choi et al. utilized the droplet microfluidic and magnetic beads to generate the hotspot by the magnetic force (Figure 2A), thus reaching the high throughput, rapid reaction, and highly efficient automatically immunoassay of specific antigen fraction 1 (F1) in *Yersinia pestis*. [5] Shamim Azimi et al. utilized the DEP force to capture the silver nanoparticle and target protein, generating the sandwich-like structure which means the target at the hotspot (Figure 2B). [6] To sum up, the SERS technique combined with the microfluidic system could gain advantages, including low sample consumption, low cost, rapid reaction, high throughput, and low detection time. Except for aggregation by the force of the microfluidics, the other functions of microfluidics could also be supplied, including molecule separation or biochemical reaction as illustrated in Figure 2C. [7] For example, Marco Becker et al. used microfluidics to concentrate the myoglobin by the isotachopheric free flow electrophoresis, in which the flow direction was perpendicular to the electric field (Figure 2D). [8] Therefore, microfluidic could help sample preprocessing in the biosensing area before SERS detection.

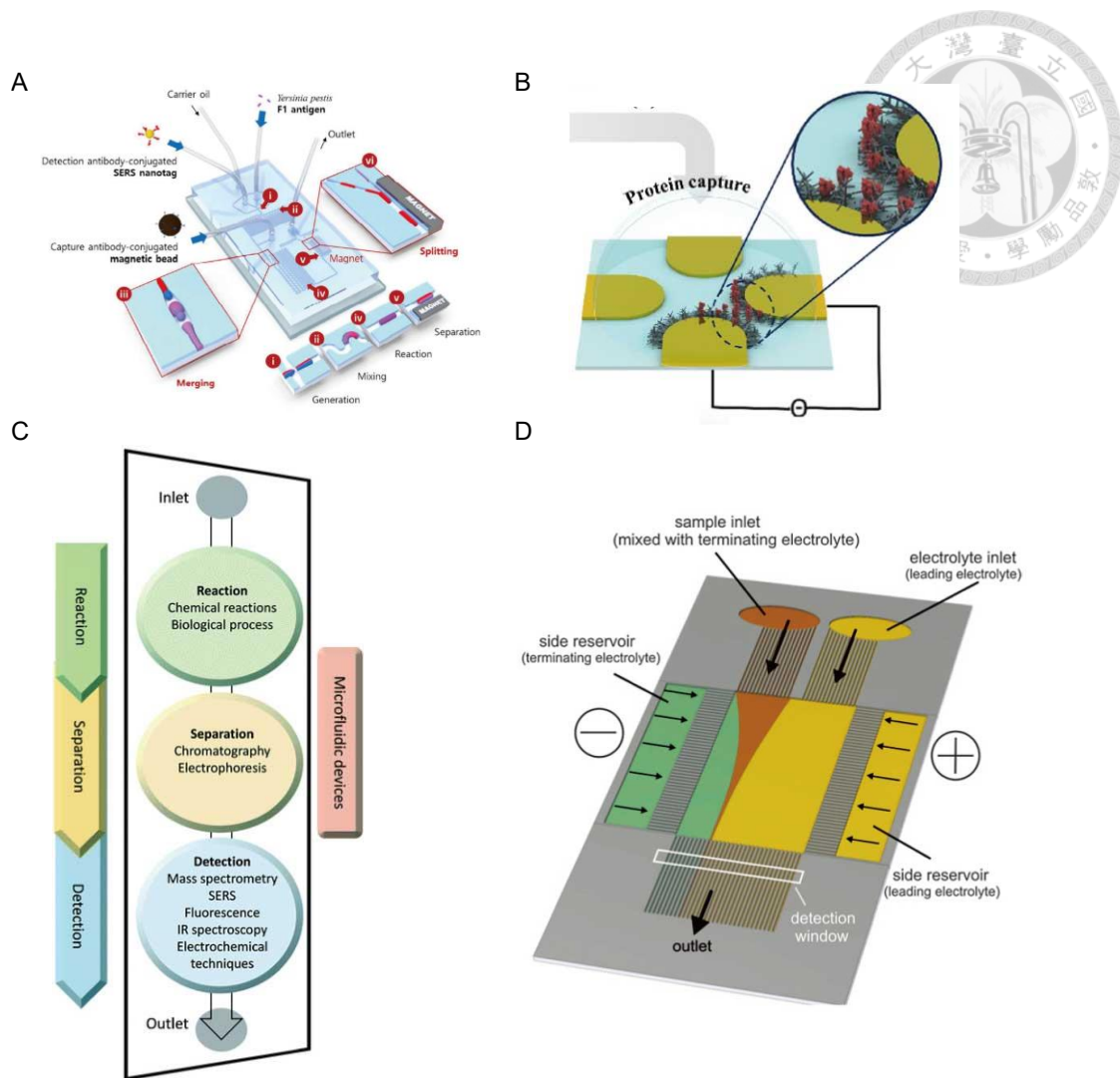
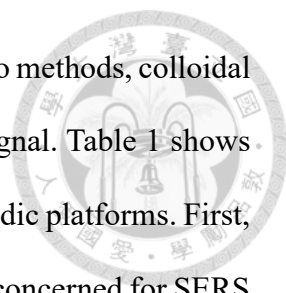


Figure 2 (A) A droplet microfluidic combines with magnetic beads for SERS hotspot generation. [5] (B) A microfluidic device combines with DEP for protein capture. [6] (C) The schematic of SERS detection in a microfluidic system. [7] (D) A microfluidic device that combines the FFE separation technique for nanoparticle aggregation. [8]

1.2 Literature Review

1.2.1 SERS in Microfluidic for Bacteria Identification

Recently, SERS has been widely utilized for bacteria identification and phenotype analysis due to its high sensitivity, specificity, and rapid detection. For bacteria identification, SERS reveal detailed information about biomolecules in the supernatant of bacteria solution, such as adenine, hypoxanthine, uracil, and other purine derivatives. [9]



In the field of surface-enhanced Raman spectroscopy, it consists of two methods, colloidal and non-colloidal types, using microfluidics to enhance the SERS signal. Table 1 shows the different research in bacteria identification by SERS and microfluidic platforms. First, for colloidal methods, the environment in the test sample needs to be concerned for SERS detection, including the ionic strength and nanoparticle concentration. B. Krafft et al. used the electrokinetic force to aggregate the silver nanoparticles and trap the bacteria at the porous membrane, therefore forming the SERS hotspot (Figure 3A). [10] A. Walter et al. used 1 M of potassium chloride and droplet microfluidics to enhance the ionic strength in the test droplet (Figure 3B). [11] Except for acquiring the bacterial supernatant which contains the purine metabolite, some research teams identify the bacteria by the bacterial DNA. J. Zhuang et al. used the CRISPR/Cas system to break the linker between the two nanoparticles. Therefore, the SERS signal could be enhanced when the target DNA was detected. [12] Although these kinds of research could reach the low limit of detection (LOD), poor reproducibility could not be avoided in this method.

Second, non-colloidal methods use evaporation deposition to deposit the nanostructure at the glass side. Although the LOD is relatively higher than the colloidal method, the reproducibility and stability could get the promise. Moreover, the preprocessing of samples would no longer be necessary in the microfluidic. For example, Y. Liu et al. injected the bacteria sample directly into the microfluidic with an RSD of 9.29%. And thanks to this, some microfluidic devices could be more colorful for different arts. K.-W. Chang used the membrane to automatically wash the bacteria in the microfluidic (Figure 3C). [13] C. C. Liao et al. used the microfluidic device for the single-cell analysis and S.-J. Lin et al. further combined antibiotic generation microfluidics for the research of antibiotic susceptibility tests (AST) (Figure 3D). [14, 15]

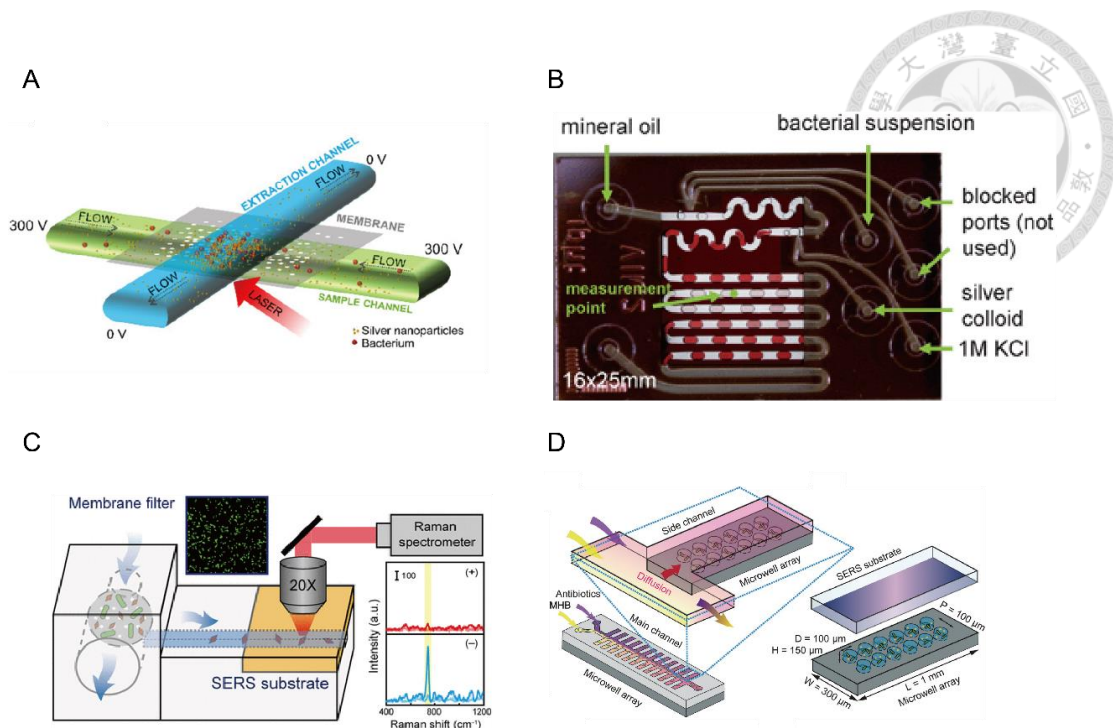


Figure 3 (A) A microfluidic device that uses electrokinetic force to concentrate nanoparticles for SERS detection. [10] (B) A droplet microfluidic that mixes KCl solution and test solution for nanoparticle aggregation and SERS detection. [11] (C) A microfluidic device for bacteria washing and SERS detection at the same time. [13] (D) A microfluidic device for antibiotic concentration gradient generation. [15]

However, SERS signals of some compounds in bacterial supernatant may overlap or be surpassed by the one with a strong affinity, making the spectrum of similar bacteria species, such as *E. coli* DH5 α WT and resistant strain which is shown in Figure 4, difficult to differentiate. For example, Anna Mühlig et al. used the PCA-LDA model to identify the *Mycobacterium* bacteria. [16] C. C. Liao et al. used the antibiotic to identify the *E. coli* DH5 α wildtype and resistant strain. Although there are many methods to identify the different SERS spectra in the bacterial supernatant, they still need large amounts of samples to train the model to remove the noise from the background and gain unexplainable results.

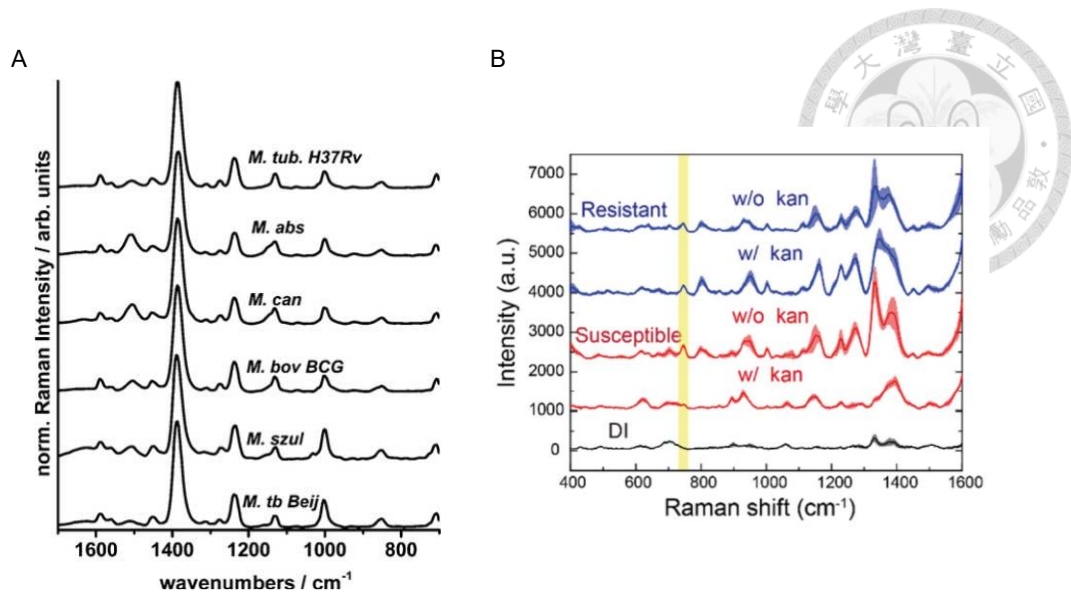


Figure 4 (A) The SERS spectrum of bacteria in the Genus of *Mycobacterium*. [16] (B)

The SERS spectrum of *E. coli* DH5 α WT and kanamycin-resistant strain. [14]

Table 1 List of several bacteria identification research by SERS and microfluidic platform

Type	Purpose	Bacteria	Analyte	Material of microfluidics	Microfluidic function	Citation
Colloidal	Rapid and point-of-need (PON) detection of bacteria	<i>Salmonella typhimurium</i>	DNA	Paper	Concentrating the nanoparticles	[12]
Colloidal	Easy-to-operate systems for the rapid and unambiguous identification of bacterial pathogens in drinking water.	<i>Escherichia coli</i> DH5 α , <i>Pseudomonas taiwanensis</i> VLB120	Purine derivative	PDMS	Concentrating the bacteria and nanoparticles	[10]
Non-colloidal	Rapid enrichment and ultrasensitive SERS detection of bacteria	<i>Escherichia coli</i> , <i>Staphylococcus aureus</i> , <i>Enterococcus faecalis</i> , <i>Bacillus subtilis</i>	Purine derivative	Customized microfluidic chip	Fluid flowing	[17]
Non-colloidal	On-chip bacterial enrichment, metabolite collection, and in situ SERS measurements for antibiotic susceptibility test	<i>Escherichia coli</i> ATCC 25922, <i>Escherichia coli</i> DH5 α Kan ^r , <i>Staphylococcus aureus</i> HG001	Purine derivative	PDMS	Washing bacteria	[13]
Non-colloidal	Rapid SERS-AST to determine the MIC of the bacteria	<i>Escherichia coli</i> BW25113, <i>Escherichia coli</i> DH5 α Amp ^r	Purine derivative	PDMS	Bacteria trapping and antibiotic gradient generation	[15]
Non-colloidal	Improve the effectiveness of early antibiotic therapy	<i>Escherichia coli</i> ATCC 25922, <i>Escherichia coli</i> DH5 α Kan ^r	Purine derivative	PDMS	Bacteria trapping and Washing bacteria	[14]



1.2.2 The Arts of Air-liquid Microfluidics

To apply air-liquid microfluidics, some research could be found and supply information on their microfluidic function and application. Table 2 shows a variety of microfluidics they designed for different purposes. For example, H. Hong et al. used T-junction-like microfluidics to generate the bubbles in the microfluidic channel, and also make the segment flow to let the liquid mix. [18] They controlled the pressure inside the syringe pump by the computer program and used the high-speed camera to capture the image of the air-liquid segment flow to calculate the size of the droplet, air resistance, and liquid resistance (Figure 5A). They derived the hydraulic resistance R_h ($N \cdot S/m^5$) that would follow Hagen-Poiseuille's law.

$$\Delta P = R_h Q \tag{1-1}$$

Where ΔP (N/m^2) represents the pressure drop, and Q (m^3/s) represents the flow rate of the channel. Finally, they mix the blue ink and yellow ink to prove the mixing efficiency and the homogeneity factor (Figure 5B).

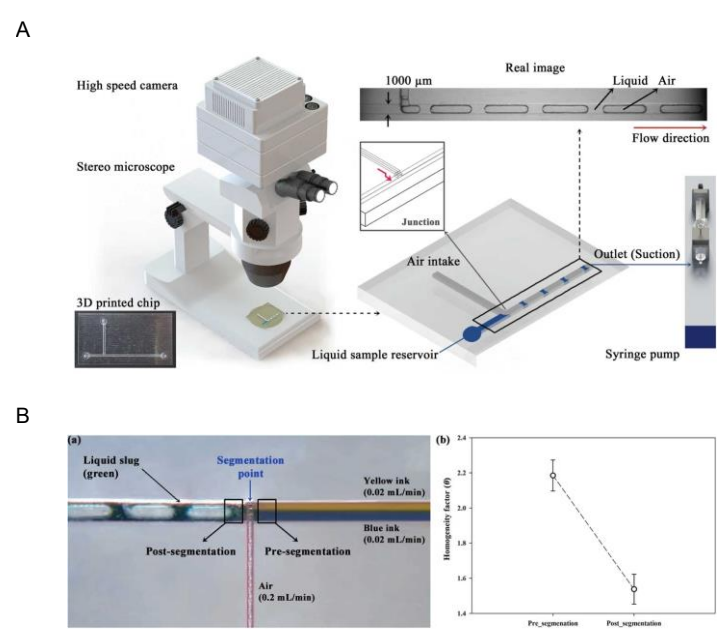


Figure 5 (A) The system setup of the T-junction microfluidics and the high-speed camera.

(B) The image of mixing results and homogeneity factor before and after mixing. [18]

Y. Song et al. used tree-like microfluidics to mimic the airway in the human body, simulating the path of droplets in Surfactant Replacement Therapy (SRT) (Figure 6A). [19] They also calculated the velocity and the resistance inside different branches of channels by measurement (Figure 6B, and C). The flow rate Q (m^3/s) was then calculated by the following equation (Figure 6D).

$$Q = Uhw \quad (1-2)$$

Where U (m/s) represents the plug velocity, h (m) and w (m) represent the height and width of the channel.

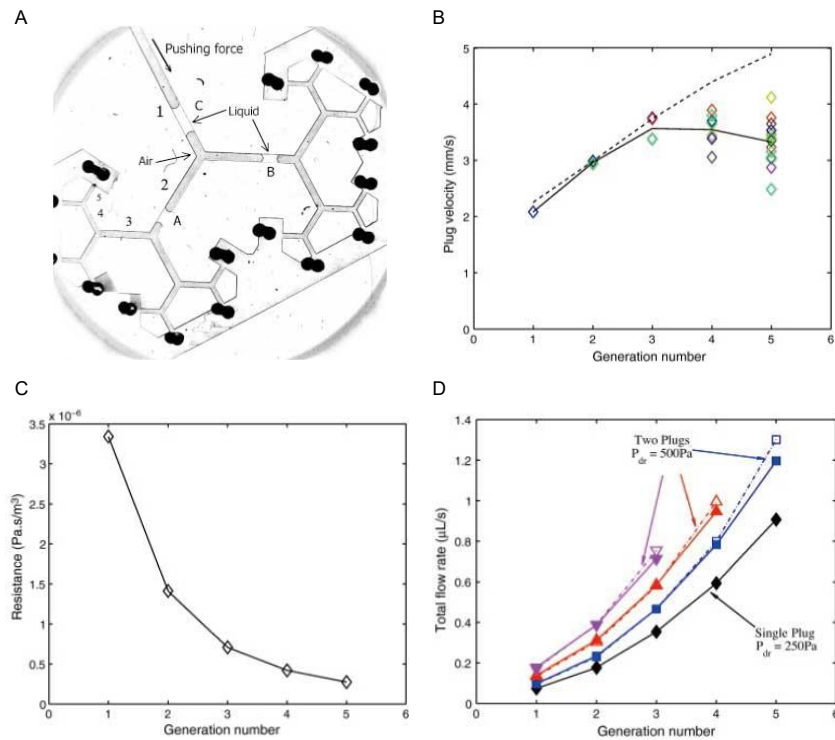


Figure 6 (A) The image of the tree-like airway microfluidics. (B) The plug velocity in each generation number. The dashed line is calculated by the previous report, while the solid line is the average velocity. (C) The resistance in each generation number. (D) The plot of the total flow rate and the generation number. [19]

D. Huh et al. used the flow-focusing method, which uses airflow to interrupt the liquid to develop a disposable flow cytometry system (Figure 7A). [20] They also found

that the sheath flow of air-liquid would have a critical flow rate to generate the droplet (Figure 7B).

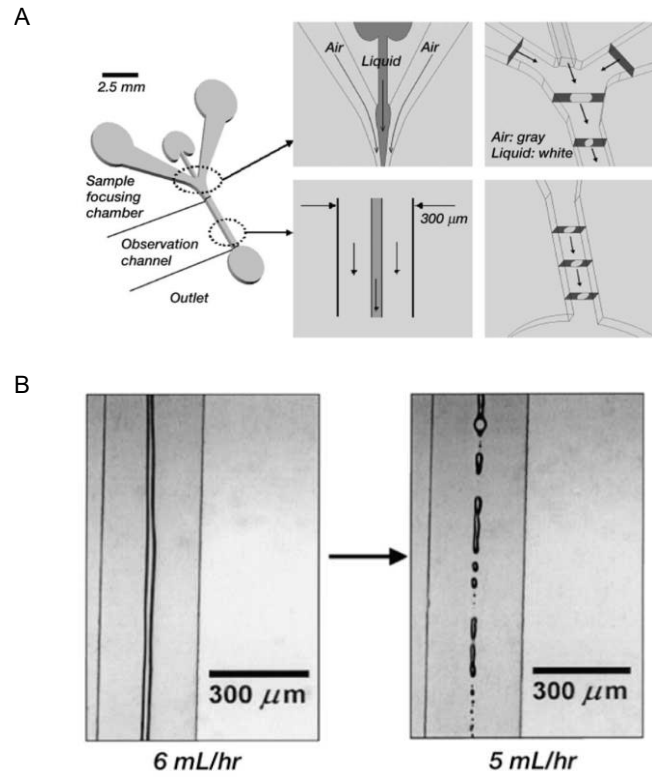


Figure 7 (A) The design of the disposable flow cytometry microfluidic system. (B) The image of the flow with the flow rate of 6 and 5 mL/hr under the constant vacuum pressure. [20]

Y. Kazoe used the Laplace valve to investigate the Weber number influencing the droplet generation (Figure 8A). [21] Briefly, the air-liquid segment flow would be interrupted when the Weber number is larger than 1, and the Laplace pressure (Pa) follows the Young-Laplace equation.

$$P_{LP} = -\frac{4\gamma \cos \theta}{D_h} \quad (1-3)$$

Where γ (N/m) represents the surface tension, θ ($^\circ$) represents the contact angle, and D_h (m) represents the hydraulic diameter. When the insert pressure was larger than the Laplace pressure, the liquid plug would move into the Laplace valve (Figure 8B).

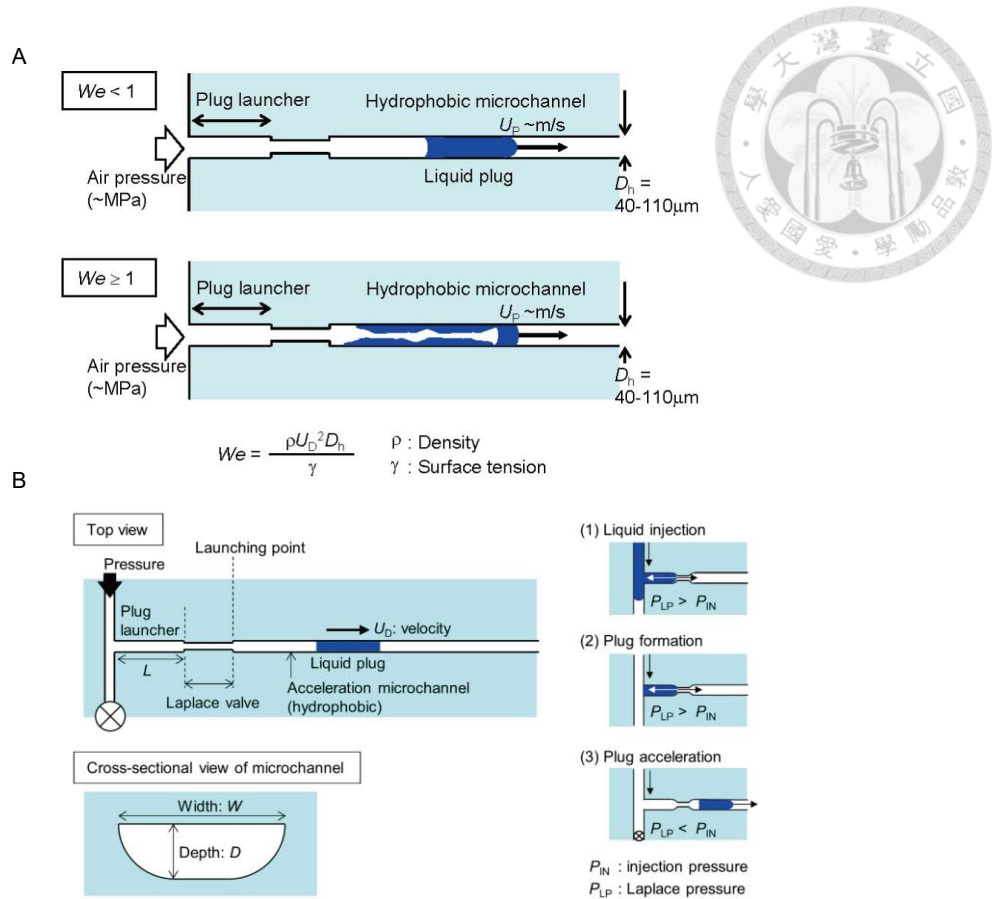


Figure 8 (A) The relationship between Weber number and the plug formation. (B) The relationship between Laplace pressure and insert pressure. [21]

T. Ishida used different hydrophobic passive microvalves to design a first-come-first-store microfluidic device for droplet storage (Figure 9A). [22] By designing different channel designs of burst pressure, including straight channel, expansion channel, and arrowhead channel, the droplet would have different actions by applying constant pressure (Figure 9B). Burst pressure ΔP_s (N/m^2) could be derived by the following equation.

$$\Delta P_s = -2 \gamma_{lg} \cos \theta_c \left(\frac{1}{w} + \frac{1}{h} \right) \quad (1-4)$$

Where γ_{lg} (N/m) represents the surface tension between liquid and gas, θ_c ($^\circ$) represents the contact angle of the air-liquid interface, and w (m) and h (m) represent the width and height of the channel.

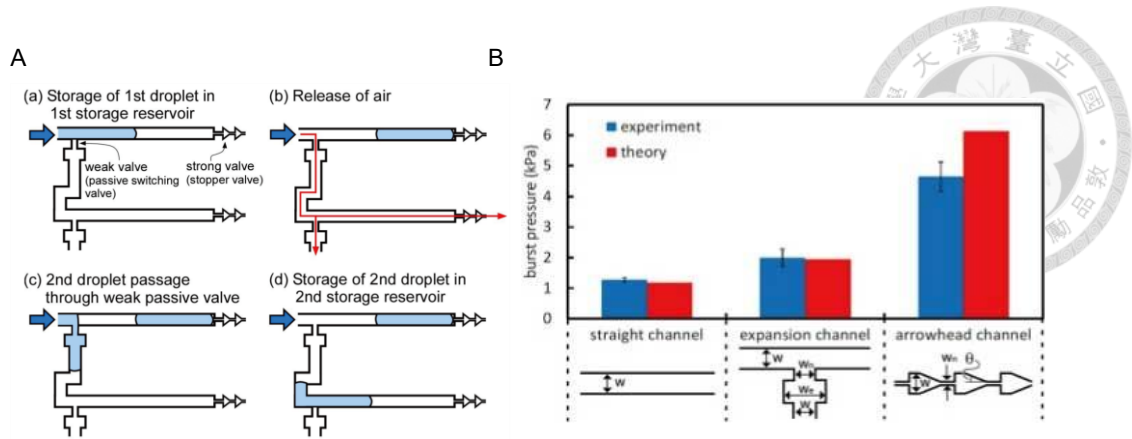


Figure 9 (A) The process of first-come-first-store microfluidics. (B) The burst pressure of different kinds of channel design. [22]

K. Kobayashi et al. used the droplet-like microfluidic design to confine the droplets inside the device and make the droplets move (Figure 10A). [23] By using the liquid selector, the color could change or the air could be inserted into the microfluidics. The pressure source they used was a vacuum pump controlled by the PC, and the pressure pattern is shown in Figure 10B. The vacuum pump supplied the impulse pressure into the microfluidics, while the pixel number increased. The pressure was contained in a stable range of 97 to 101 kPa. They first designed different kinds of designs to evaluate the volume loss as shown in Figure 10C. They defined the volume loss by the following formula.

$$W_{loss}(n) = \frac{V(0) - V(n')}{V_{pixel} \cdot n'} \cdot n \quad (1-5)$$

Where n and n' are the pixel number which is the independent variable and experimental constant, respectively, and $V(n)$ (m^3) means the volume of droplets inside the channel along the n pixels. V_{pixel} (m^3) is the volume of the microchannel. They found that the volume loss at the wellhead of 60° would have the minimum (red bar) even in different heights and widths of the channel. For both type A ($d = 800 \mu m$) and type B ($d = 400 \mu m$) designs, the width (w) to diameter (d) ratio was controlled at 1:4. The results show that

the 200 μm height and type A design could save the volume loss the most. For the situation of different amounts of droplet sizes, the pressure supplied by the vacuum pump also needed to be doubled or more times than pushing a single droplet. Because of the elasticity of the PDMS, the microfluidic device also could bend with the external force. Although there would have been slightly disturbed when the display was bent, the image was recovered when the display was returned to the initial flat condition.

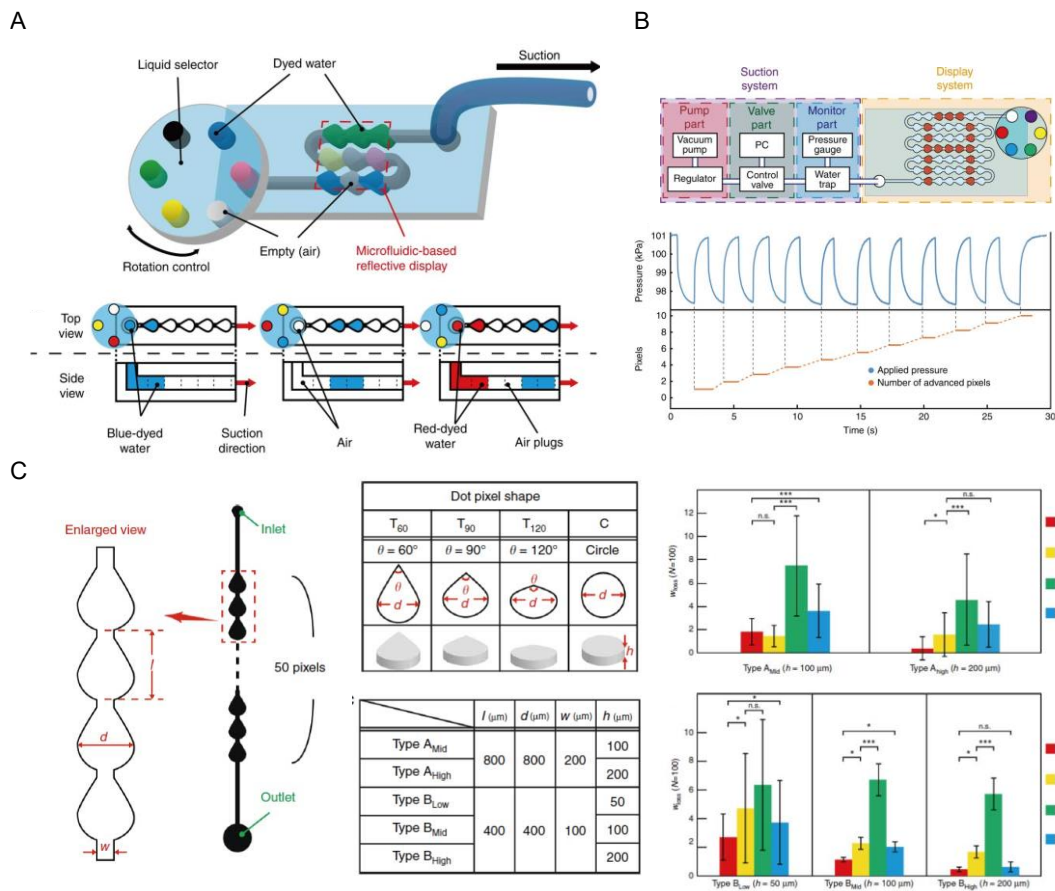
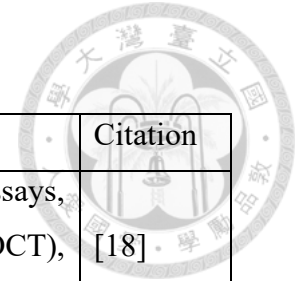


Figure 10 (A) The schematic of the microfluidic-based multicolor display. (B) The pattern of pressure supplied by the vacuum pump and monitored by the PC. (C) The volume loss evaluation under the different kinds of design and channel width and height. [23]

Table 2 List of several air-liquid microfluidic research



Purpose	Pump	Shape of microfluidics	Channel width	Application	Citation
Droplet generation and mixing	Syringe pump	T-shape	1000 μm	Sensitive diagnostic assays, point-of-care testing (POCT), compact liquid-handling pump	[18]
Droplet division	Pressure pump + Syringe pump	Y-junction	Largest 720 μm	Simulation of Surfactant Replacement Therapy	[19]
Droplet generation	Pressure pump + Syringe pump	Y-junction	300 μm	Space-saving and disposable flow cytometry system	[20]
Droplet moving	Custom-made pressure-driven fluid control system	T-shape	70~200 μm	Design guidelines for achieving the stable transport of a micro liquid plug	[21]
Droplet storage	Pressure source	Straight channel Expansion channel Arrowhead channel	100 μm	Highly sensitive chemical analysis and measure the temporal concentration change of target chemicals	[22]
Droplet moving	Vacuum pump	Droplet and circle	100, 200 μm	Multicolor display	[23]

1.2.3 Adsorptive Separation and Bacterial Supernatant

Adsorptive separation describes the method that binds the impurities and filters out the clean solution, especially the water. Therefore, it usually appears in the field of membrane filtration. [24] Nowadays, the appearance of graphite increases the curiosity of people to investigate the phenomenon of adsorptive separation. It is a low-energy method to purify the water because of the characteristic of high hydrophobicity, large delocalized π - π electron system, and large surface area (up to $2600 \text{ m}^2 \text{ g}^{-1}$). [25] The process is also easy to conduct as shown in Figure 11.

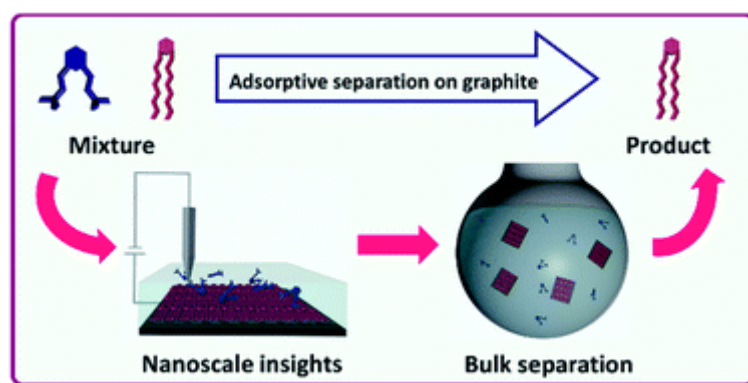


Figure 11 The illustration of adsorptive separation. [25]

By the same conception, when it comes to the complex composition sample, like the bacterial supernatant which is composed of purine derivatives. Different types of bacteria have different enzymes, meaning that they have different pathways to digest the purine (Figure 12A), finally showing the different SERS spectrum in Figure 12B.

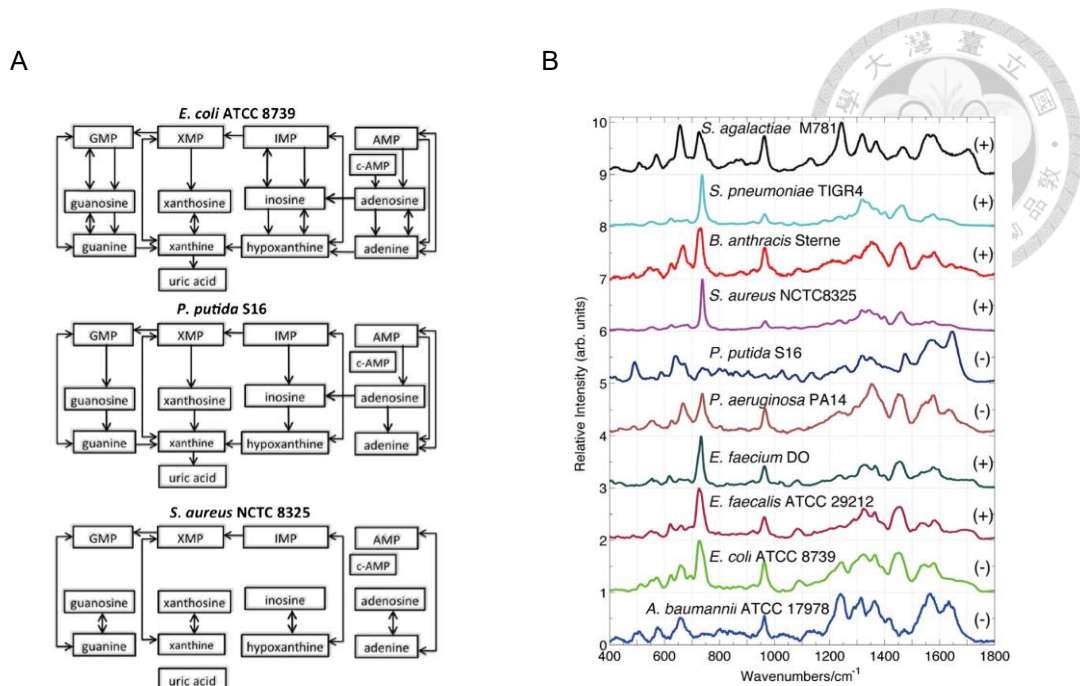


Figure 12 (A) The purine metabolic pathways of different bacteria. [9] (B) The SERS spectrum of different bacterial supernatants. [9]

For bacterial identification, the most appeared in the SERS spectrum analyte is adenine which is one of the purine derivatives. Research using the density function theory (DFT) method to analyze the relationship between the adenine and silver surface. They found that the adenine could act as the nucleophile to interact with the metal surface, providing the active site as Lewis acid and interacting by the electrostatic potential as shown in Figure 13. Therefore, it is a good candidate for us to judge the parameters in the experiments.

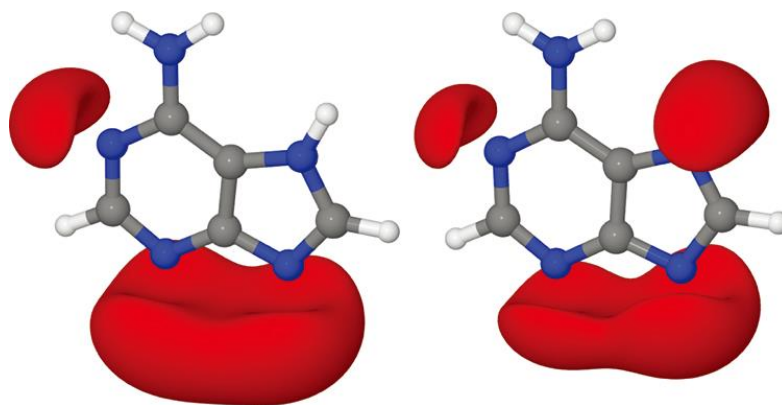


Figure 13 The DFT simulation of adenine bonding with silver surface. [26]

Some research also depicted other biomolecules interacting with the metal surface by DFT. In comparison to adenine, the interaction between pyrimidine and the metal surface is weaker as shown in Figure 14A and B. [27, 28] A study also indicated that catechol-based molecules have a lower affinity with silver substrate than the indole-based molecules as shown in Figure 14C. [29]

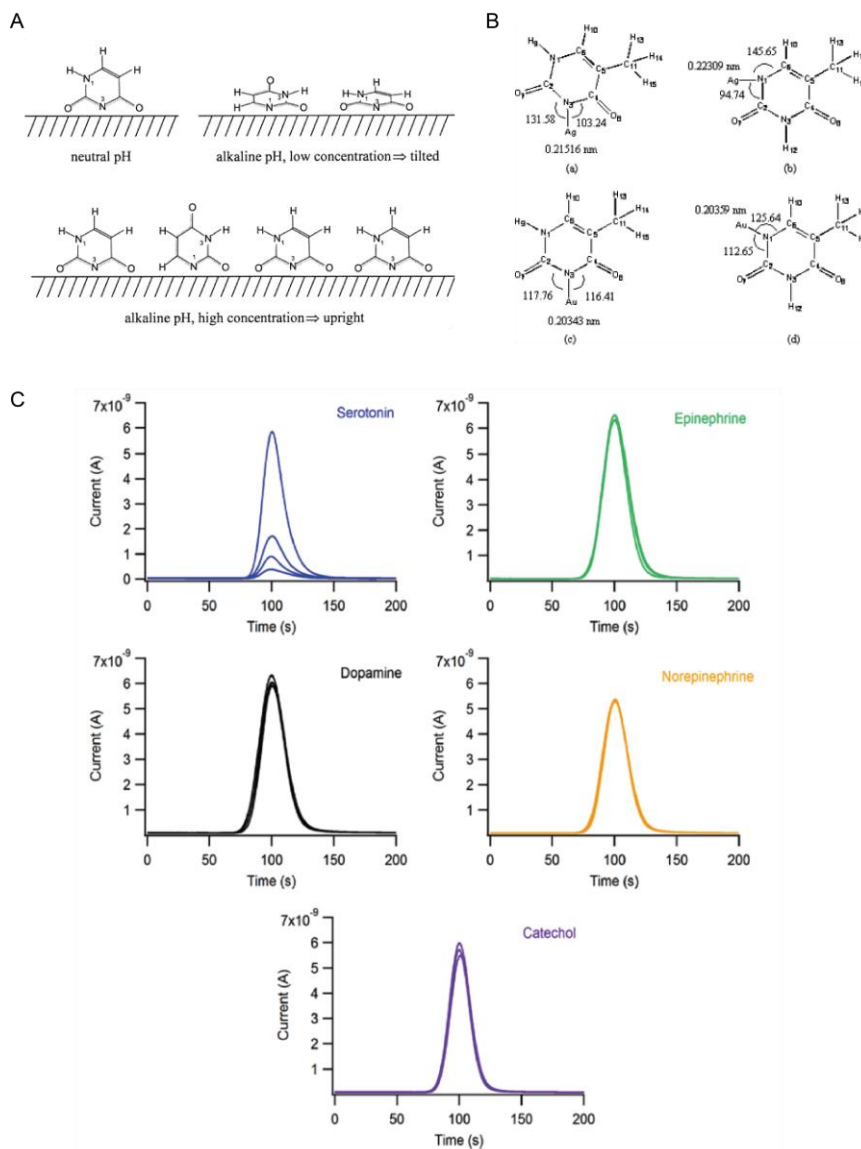


Figure 14 (A) The uracil binds with the silver surface at different pH values. [28] (B) The thymine binds with the silver surface in different forms. [27] (C) The electrochemical reaction of serotonin, epinephrine, dopamine, norepinephrine, and catechol with different running times. [29]

1.3 Research Motivation



In this thesis, we aim to use air-liquid microfluidics to distinguish the same types of bacteria that may share a similar SERS spectrum mentioned. By integrating the silver-nanostructure SERS substrate, different compounds could be separated by their different affinity to the silver surface. To achieve this concept, we flowed and stopped the sample solution in the air-liquid microfluidics by the pressure pumping system. When the sample solution flowed through each well, in-situ SERS measurement was recorded. Therefore, small peaks that hide from the main peak could be observed, and sample solutions that initially seem the same could be differentiated by those small peaks. In the results part, we first fabricated the microfluidic device to evaluate the sample volume loss from the microfluidic channel. To optimize the microfluidic design and match the theory of air-liquid interface, we designed different channel widths of microfluidics to evaluate the volume loss. Once the 2D design of microfluidics was determined, the reaction time and the channel height were then decided because they might influence the SERS signal and attenuation curve. Different biomolecules that might appear in bacterial supernatant were then evaluated by our system and defined as high-affinity and low-affinity, and then mixed for proof of concept. Finally, we introduced the bacterial supernatant into our microfluidic system to fit the situation, helping the doctor quickly determine the antibiotics to use in patients with bacterial infections. To sum up, we fulfilled and constructed an air-liquid microfluidic system that combined the SERS active substrate for automatically controlling the droplet position in the well and automatically acquiring the SERS spectrum. Also, we defined the affinity of the biomolecules to the silver surface. Finally, we expanded the data of a single droplet into big data, causing higher accuracy in machine learning.

Chapter 2 Theory

2.1 Raman Scattering

Many kinds of measurement methods can be found in modern optical detection, including fluorescence and phosphorescence. These methods can be categorized into two types, elastic and inelastic scattering. Elastic scattering of light such as Rayleigh scattering occurs when the light is scattered by the dust or other nanoparticles without any energy loss and wavelength change. Inelastic scattering such as Raman scattering, in contrast, would cause energy loss and wavelength change. From the views of quantum mechanics depicted in Figure 15, the molecule will be induced to a virtual energy state when the photon interacts with the molecule. However, the molecule will then relax into the initial ground state or higher or lower than the initial ground state. Rayleigh elastic scattering is the one that will relax into the initial ground state. On the other hand, Raman inelastic scattering which relaxes into higher than the initial ground state is called Stokes Raman scattering, and lower than the initial ground state is called Anti-Stokes Raman scattering. In biomedical analysis, most molecules would undergo Stokes Raman scattering within one of 10^8 photons.

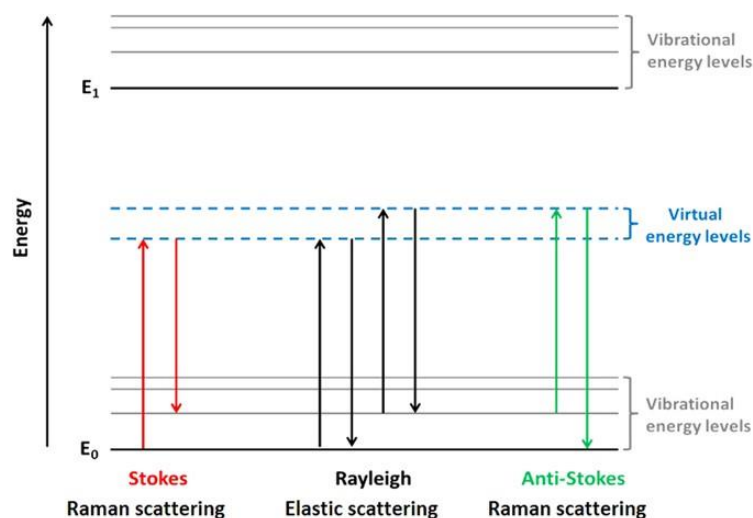


Figure 15 The principle of Raman scattering. [30]

A Raman spectrum is the plot of Raman intensity and Raman shift. The Raman intensity which is the vertical axis in Raman spectra is proportional to the number of scattering molecules. The number of scattering molecules follows the Boltzmann distribution.

$$N_1/N_2 = (g_1/g_2)\exp [-\Delta E/KT] \quad (2-1)$$

Where N_1 and N_2 represent the number of molecules in higher and lower levels, and g_1 and g_2 represent the degeneracy of higher and lower levels. ΔE (J) is the energy change before and after the scattering. K is Boltzmann's constant (1.38×10^{-16} J/K), while T (K) represents the temperature.

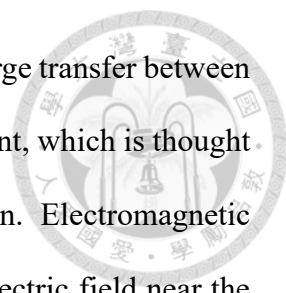
The Raman shift which is the horizontal axis in Raman spectra is proportional to the frequency and relative to the incident laser excitation. The Raman shift (cm^{-1}) can be determined by

$$\text{Raman shift} = \left(\frac{1}{\lambda_{\text{incident}}} - \frac{1}{\lambda_{\text{scattered}}} \right) \times 10^7 \quad (2-2)$$

Where $\lambda_{\text{incident}}$ and $\lambda_{\text{scattered}}$ (nm) represent the wavelength of incident light and scattered light. Different position of Raman shift represents the vibration or stretching between the different molecule and molecule. For instance, 727 cm^{-1} of Raman shift represents the C-C stretching. Therefore, each compound would have a unique "fingerprint". We can use this kind of feature to identify the composition in the unknown test solution as Raman intensity has a linear relationship to the concentration of the molecule. Raman spectra could also apply different phases of compounds, including solid, liquid, and gas. [31]

2.2 SERS Theory

Surface-enhanced Raman spectroscopy (SERS) utilizes noble metal nanoparticles to enhance the Raman intensity by a factor of $10^6 \sim 10^8$. There are two kinds of mechanisms that could cause this phenomenon. One is chemical enhancement as shown in Figure 16.



It can enhance Raman intensity by a factor of $10^2 \sim 10^3$ because of charge transfer between the analyte and substrate. Another one is electromagnetic enhancement, which is thought to be the main reason that causes the enhancement phenomenon. Electromagnetic enhancement occurs when local surface plasmons concentrate the electric field near the surface of the metal nanoparticle, like the lightning rod effect, and induce the “hot spot” located at the edge of the metal nanoparticle. This phenomenon is the so-called Localized Surface Plasmon Resonance (LSPR). Thus, it can enhance Raman intensity by a factor of $10^8 \sim 10^{11}$. The way that caused LSPR can be divided into two groups. One is using the metallic nanostructure on the substrate by the lithography. Another one is using the colloidal nanoparticles suspension on the test solution. The advantage of using colloidal nanoparticles is that they can reach the low limit of detection (LOD), but the stability is relatively low and the ionic strength may influence the nanoparticle aggregation. The advantages of using the metallic nanostructure include low signal-to-noise ratio, stability, and high reproducibility. The choice of metal nanoparticles is roughly gold and silver. The gold nanoparticle has biocompatibility and easy functionalization characteristics, but the SERS signal is relatively low. The silver nanoparticle can gain the largest SERS signal as long as the silver nanoparticle is stored in a vacuum and low-temperature environment avoiding oxidation.

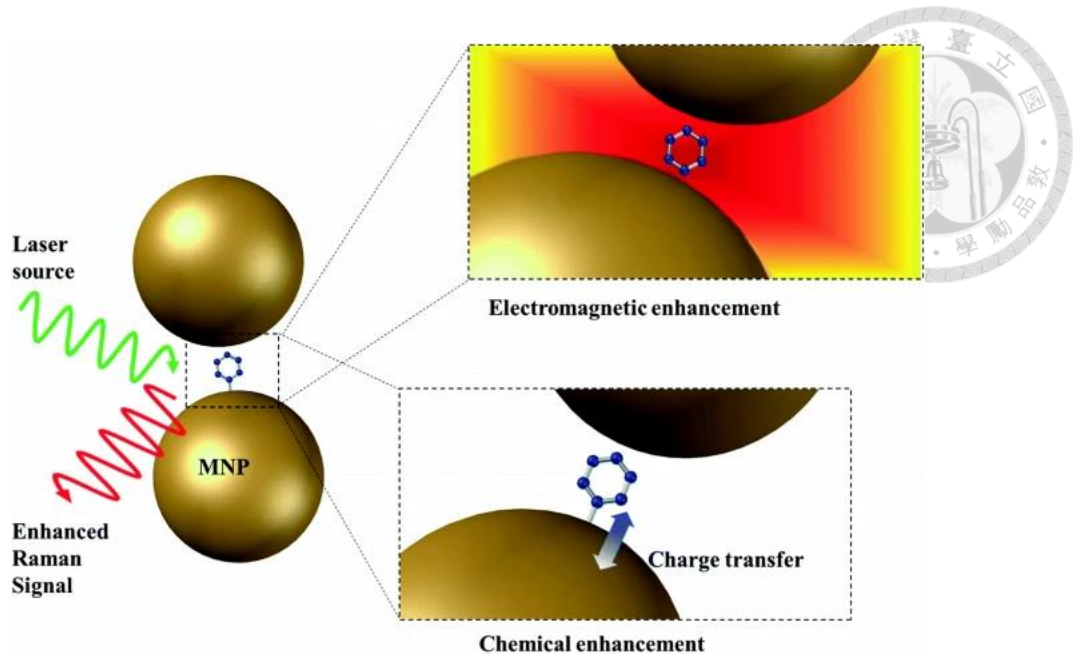


Figure 16 The electromagnetic enhancement and chemical enhancement in the SERS mechanism. [32]

2.3 The Behavior of the Air-Liquid Interface

The detection and measurement of some biomarker or molecule in the bio-diagnosis field is a critical parameter that judges a patient whether they have a disease. The type of sample is usually in the liquid phase, so some research processing the liquid such as a microfluidic chip came out. To drive the air-liquid microfluidic for saving the sample volume, the study of the behavior of the air-liquid interface is important to realize the principle and mechanism in design. The parameter that determines whether the droplet spitted or not is Weber number. The Weber number can be calculated using the following formula.

$$We = \frac{\rho U_D^2 D_h}{\gamma} \quad (2-3)$$

Where ρ (kg/m^3) stands for the density of liquid and γ (N/m) represents the surface tension of liquid. U_D (m/s) is the velocity of liquid and D_h (m) is the hydraulic diameter. As shown in Figure 17, the droplet in the microfluidic would not split if Weber number is smaller

than 1. On the other hand, the droplet would split when the Weber number is larger than and equal to 1.

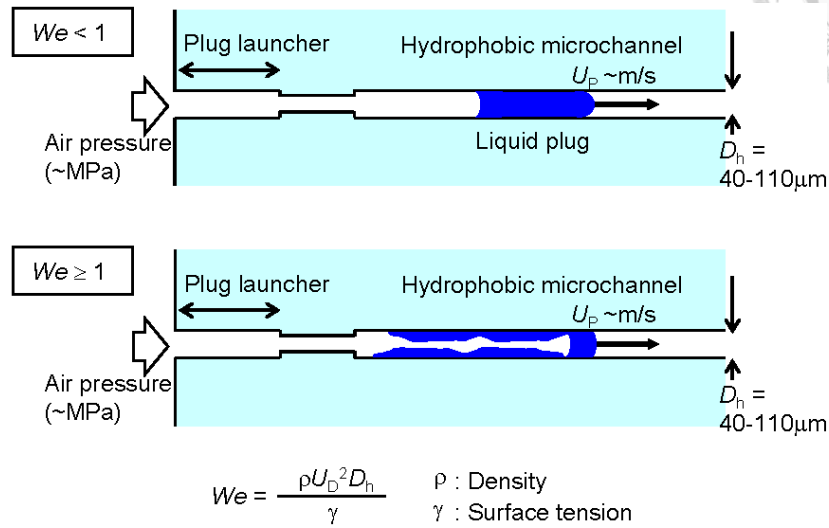


Figure 17 The relationship between Weber number and air-liquid flow. [21]

Another parameter that can influence the design of microfluidics is the contact angle between the liquid phase and gas phase (Figure 18). The contact angle can be determined by the following formula.

$$F_L = \frac{2\gamma V \cos\theta}{d^2} \quad (2-4)$$

Where F_L (N) represents the force of liquid, γ (N/m) represents the surface tension of liquid. V (m^3) is the volume of the droplet, and d (m) is the gap between two solid surfaces.

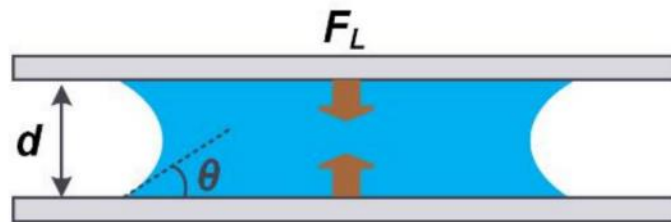


Figure 18 The relationship between the contact angle and the gap between two solid surfaces. [33]

Chapter 3 Materials and Methods



3.1 Reagents

The Fluorescein isothiocyanate (FITC) was purchased from Sigma Aldrich for the evaluation of microfluidic chip performance. Rhodamine 6G was purchased from ACROS Organics for measurement of enhancement factor. Adenine, guanine, cytosine, and thymine were purchased from ACROS Organics. Hypoxanthine and uracil were purchased from Sigma Aldrich for SERS detection. The PDMS 184A and 184B were purchased from SILMORE for the fabrication of a microfluidic chip.

3.2 Bacteria Incubation and Supernatant Extraction

Bacteria samples including *Bacillus subtilis* ATCC 6633, *Escherichia coli* BW25113, *E. coli* BL21, *E. coli* DH5 α WT, and *E. coli* DH5 α Amp^r which is transfected with the pGS-21 gene and has resistance to ampicillin were used in the experiment. *E. coli* BW25113, BL21, and *Bacillus subtilis* ATCC 6633 were purchased from the American Type Culture Collection. *E. coli* DH5 α WT was purchased from Yeastern Biotech. The bacteria stock solution was prepared by mixing with 0.5 mL of overnight bacterial culture and 50% sterile glycerol solution of 0.5 mL in a 1.5 mL microtube. These different types of bacteria samples were stored in a refrigerator at -80 °C. Bacterial culture was prepared by adding 0.5 μ L bacterial stock solution and 5 mL Mueller Hinton Broth (MHB) which was purchased from BD and incubated at 37 °C with 200 rpm for 18 hours.

For supernatant extraction, the overnight bacterial culture was refreshed with a new MHB solution, and then adjust the concentration to 5×10^8 CFU/mL (O.D.₆₀₀ = 0.5). The 1 mL refreshed bacterial solution was then added into 1.5 mL Eppendorf and centrifuged at 14800 rpm for 2 mins. After replacing the 900 μ L supernatant with 900 μ L sterile DI water and pipetting up and down for resuspension, the bacterial solution was centrifuged

at 14800 rpm for 2 mins again twice to replace the broth solution into DI. By replacing 900 μL supernatant with 100 μL sterile DI water, the concentrated bacterial solution in 200 μL DI water could be gained and then incubated in a 37 °C oven for 30 mins. Therefore, purine metabolites could be extracted from bacterial culture by centrifuging at 14800 rpm for 2 mins and extracting the supernatant.

3.3 Device Design and Fabrication

The microfluidic device design is shown in Figure 19. According to previous research, the wellhead of 60° would save the volume loss the most. [23] Based on this result, we designed the chip with different channel widths for further experiments as shown in Figure 19A-C. Simply, the inlet diameter and outlet diameter would be set at 1.5 mm and 2.5 mm respectively. The gap between each well would be set at 1 mm because of the limitation of the CNC machine. After deciding the channel width of 0.4 mm and height of 0.3 mm, the final design is shown in Figure 19D which can save the space of the SERS substrate and expand the regions to adsorb the molecules in the droplet.

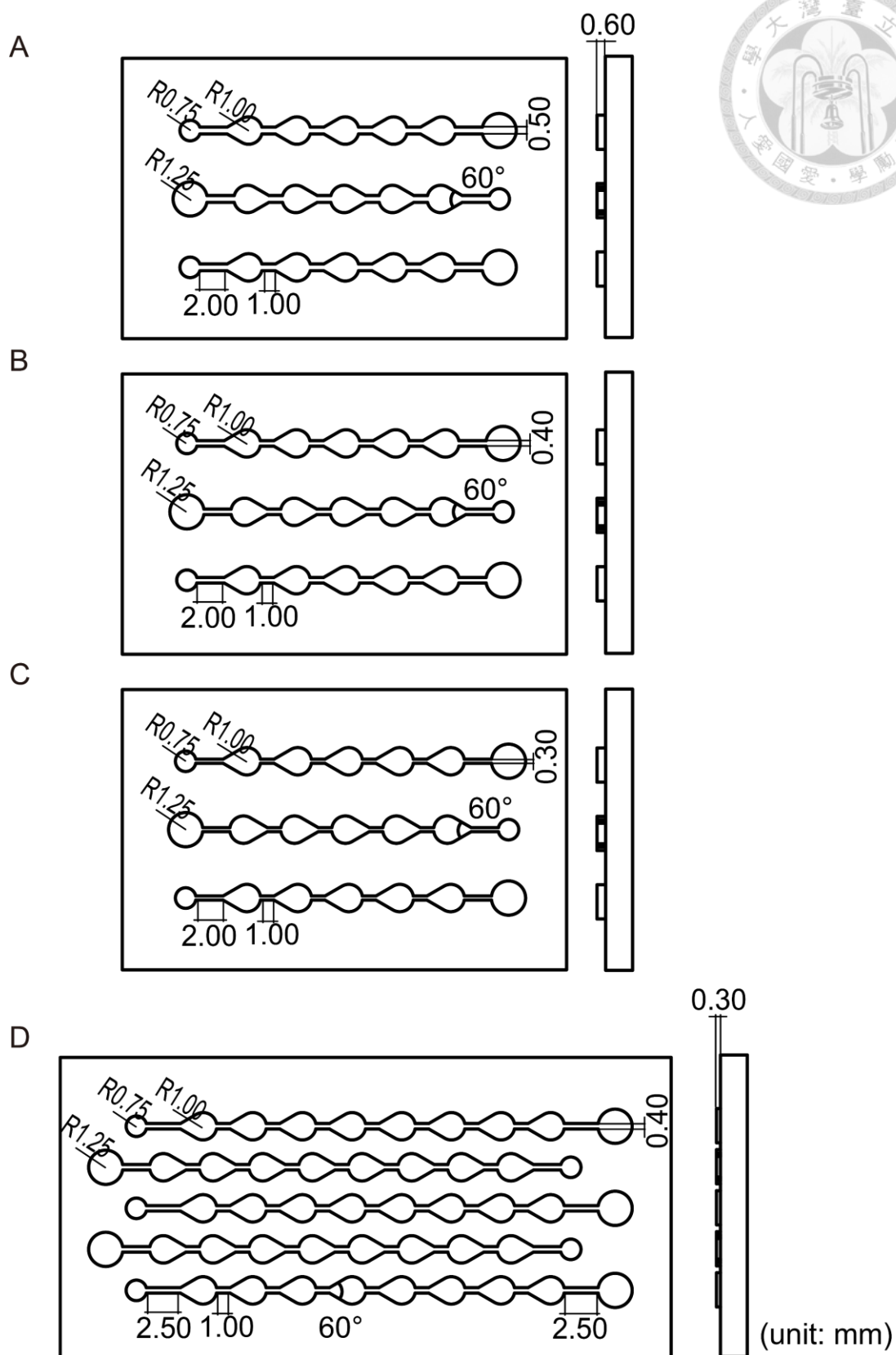
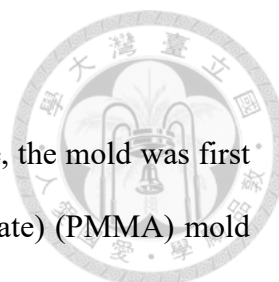


Figure 19 The design of the microfluidic chip with a channel width of (A) 0.5 mm (B) 0.4 mm (C) 0.3 mm. (D) The final design of the microfluidic chip used for the SERS detection.



3.3.1 Mold Fabrication

To make the polydimethylsiloxane (PDMS) microfluidic device, the mold was first needed to let the cured PDMS flip out. The poly (methyl methacrylate) (PMMA) mold was chosen and crafted by computer numeric control (CNC) machine, Roland MDX-50 (Figure 20A) and Roland EGX-400 (Figure 20B), because of easy fabricating and low cost. On the other hand, the height of the channel was not smaller than 100 μm . Therefore, it was the reason why the SU-8 standard photolithography process was not chosen. The process of CNC milling started with the design work of chips by the software SOLIDWORKS 2019. The pathway setting was then completed with the VISI software. The 0.5 mm drill would start moving with a spin rate of 15000 rpm to cut the region 0.4 mm outside the main region and the 0.3 mm drill would then cut to the main region with a spin rate of 15000 rpm for Roland MDX-50. For Roland EGX-400, the 0.5 mm drill would start with a spin rate of 23000 rpm to cut to the main region.

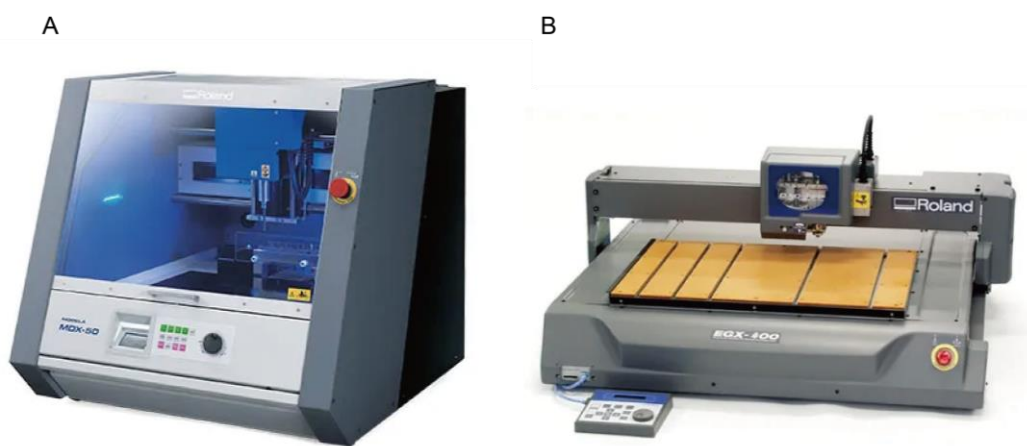
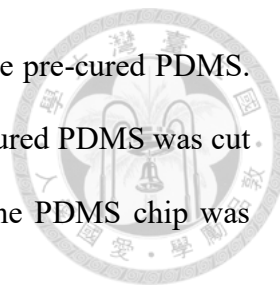


Figure 20 The CNC machine of (A) Roland MDX-50 (B) Roland EGX-400.

3.3.2 PDMS Chip Fabrication

The fabrication of the PDMS chip was followed by the standard soft lithography method. Briefly, the monomer and curing agent with a weight ratio of 10:1 was mixed and degassed by the desiccator. The degassed PDMS was poured into the PMMA mold

in the Petri dish and again degassed to remove the bubbles inside the pre-cured PDMS. After placing the pre-cured PDMS in a 60 °C oven for 4 hours, the cured PDMS was cut from the Petri dish and flipped out of the PMMA mold. Finally, the PDMS chip was punched by biopsy punch for the inlet and outlet.



3.4 Combination of SERS Substrate and PDMS Chip

Nowadays, there is a difficulty that combining the deposition-made SERS substrate and PDMS microfluidics. Some research used methanol as a lubricant and then binding by oxygen plasma. [34] Some research discarded the deposition method and tried electrodepositing metal nanoparticles inside the channel. [29] However, the SERS intensity would lose or be less than the original deposition method. Therefore, it is necessary to find a way to combine these two kinds of objects to gain the maximum benefits.

For the combination of SERS substrate and PDMS chip, the PDMS was prepared by monomer and curing agent with a weight ratio of 10:1 and then degassed by the vacuum desiccator. Next, 0.5g of pre-cured PDMS was poured on the petri dish, and spin-coating with a pre-spin rate of 500 rpm for 10 seconds and a spin rate of 3000 rpm for 30 seconds. According to previous research, the PDMS film could be lower than 25 μm . [35] A cured PDMS microfluidics was then placed on the petri dish and stuck on the SERS substrate by using PDMS film as glue. The PDMS chip and SERS substrate were subsequently put into the slide box and vacuumed by the vacuum package machine to prevent the SERS substrate oxidation. After packaging, the chip was placed into a 60 °C oven for 4 hours to let the PDMS film cure. Finally, the chip was stored at a -20 °C refrigerator. The overall schematic is illustrated in Figure 21.

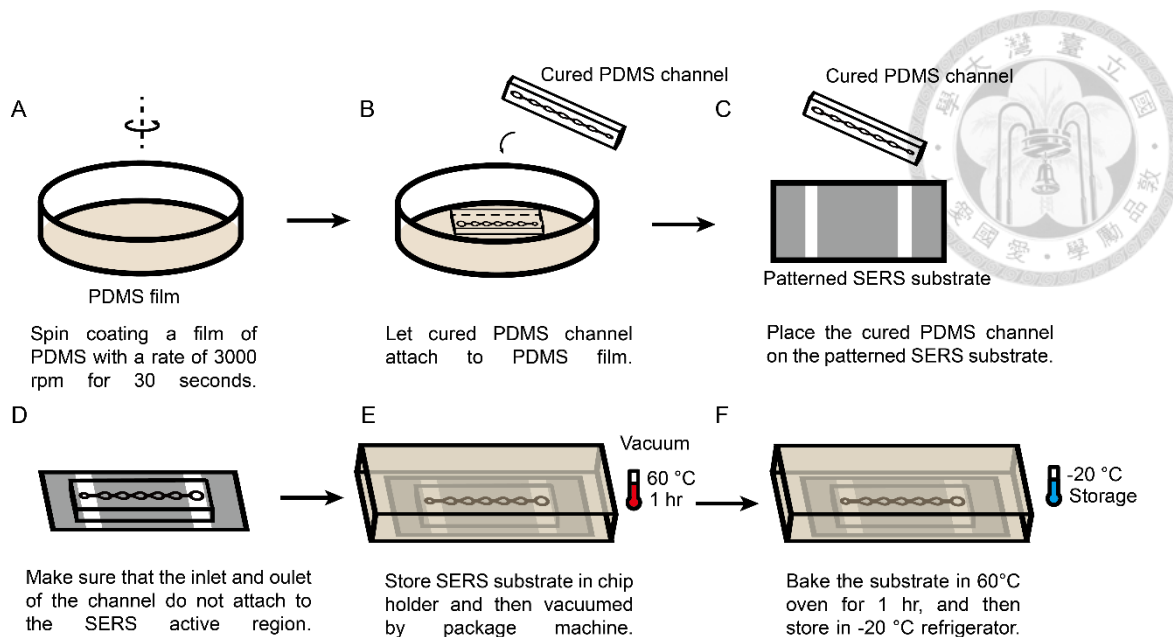


Figure 21 The process of chip fabrication.

3.5 Pressure Pumping System

The pressure pump (OB1, ELVEFLOW) illustrated in Figure 22A was used to supply the impulse of flow rate which is illustrated in Figure 22B. Before connecting any tube, the pressure pump was calibrated by the ESI software. The setup of the pressure pumping system is illustrated in Figure 22C, the pressure pump supplied the pressure to a Falcon tube and pushes the solution into the flow sensor, therefore, the relationship between pressure and flow rate could be built and real-time adjust the change by the function in the software. We dropped the test solution into a microfluidic chip and then removed the fluid after the flow sensor, finally connected to the microfluidic chip. The parameters of the pressure pump shown in Table 3 were set by the software. We set the lowest flow rate at $-5 \mu\text{L}/\text{min}$ which would stop the droplet from moving in the microfluidic, and then change the highest flow rate to fit the droplet position in the well. The duration was set at approximately 3 minutes.

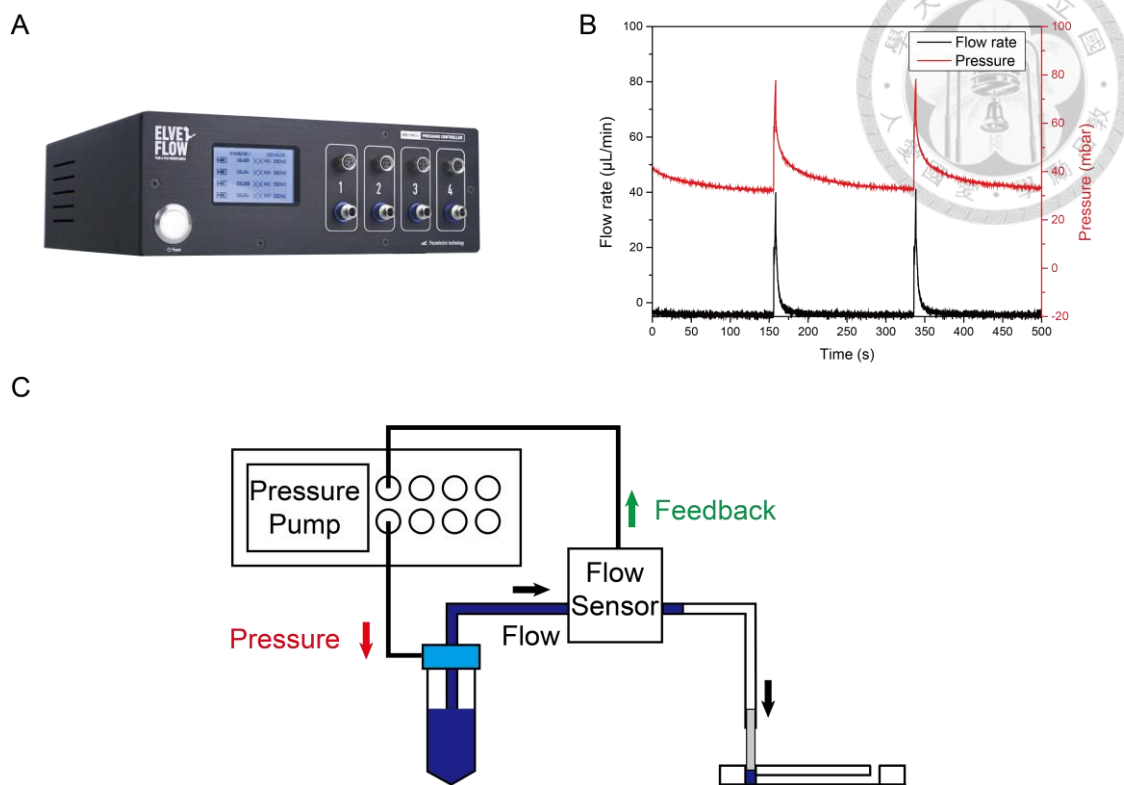


Figure 22 (A) The image of the pressure pump. (OB1) (B) The flow rate and pressure reported from OB1 and the flow sensor. (C) The schematic of the pressure pump setup.

Table 3 The parameters of the pressure pump.

For a channel height of 600 μm			
Period (min)	1	3	5
Highest flow rate (μL/min)	120	160	180
Lowest flow rate (μL/min)	-5	-5	-5
Asymmetry	-0.9	-0.97	-0.98
Duration (s)	3	2.7	3

$$Duration = \frac{Period}{2} (1 + Asymmetry) \quad (3-1)$$

3.6 The Optical and Fluorescent Microscope

The inverted fluorescence microscope (IX-73, Olympus) was equipped with a dual-color charge-coupled device (CCD) camera (DP-80, Olympus) and a CMOS camera (ORCA V3, Hamamatsu). The objective lens includes 2X, 4X, 10X, 20X, and 40X (PlanN, Olympus). The software of Cellsens controls the stitching image, exposure time, and motorized stage (Mashausr, MFD-2). The blue light filter was used to excite the fluorescent compound. (Excitation: 460~495 nm; Emission: 510 nm up) The final image was analyzed by the software of ImageJ.

3.7 SERS Measurement

3.7.1 SERS Substrate

SERS substrate was fabricated by Professor Yuh-Lin Wang's Lab, Institute of Atomic and Molecular Science, Taiwan. Briefly, the substrate was made by two-step processes, glass slide washing, and evaporation deposition. In the step of glass slide washing, the glass slide was firstly washed with acetone in the ultrasonic cleaner, and then washed with hydrofluoric acid and methanol. The glass slide was rinsed by DI between each step and finally dried out with a nitrogen gun. In the step of evaporation deposition, the E-gun evaporator (EBS-300, JunsunTech) was used with an evaporation rate of 0.05 Å/sec and a thickness of 7 nm. During the evaporation, the pressure inside the chamber was maintained at 3×10^{-6} Torr and the temperature of water cooling was kept at 20°C. The SEM image of the SERS substrate is illustrated in Figure 23A, and the enhancement factor was calculated by the following formula by detecting the Rhodamine 6G solution as shown in Figure 23B.

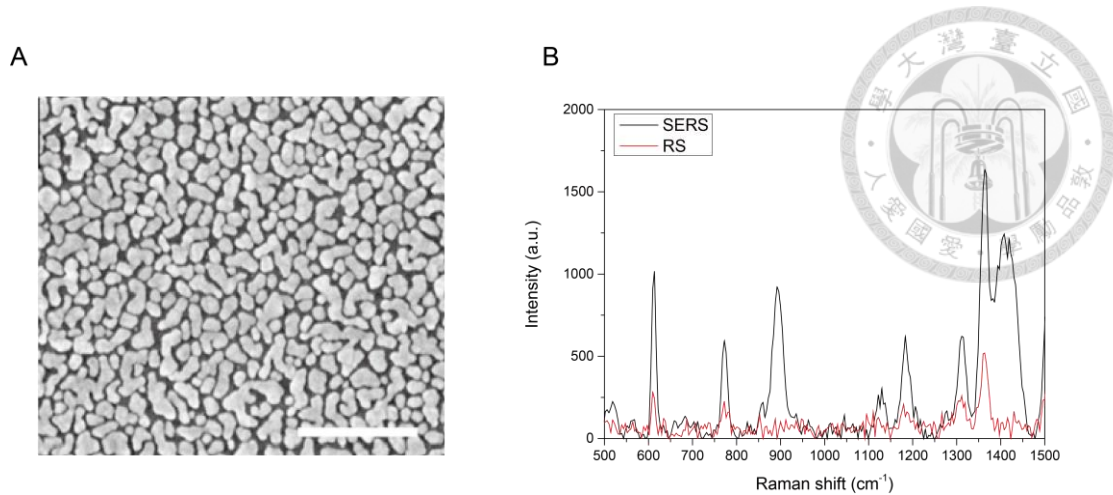


Figure 23 (A) The SEM image of the SERS substrate (scale bar = 200 nm). [13] (B) The SERS spectrum and Raman spectrum of Rhodamine 6G solution in a concentration of 10^{-6} M and 10^{-2} M, respectively, and $EF = 4.17E4$.

$$EF = \frac{I_{SERS}}{I_{Raman}} \times \frac{N_{Raman}}{N_{SERS}} \quad (3-2)$$

Where I (a.u.) represents the intensity of the spectrum signal, while N (M) represents the concentration of the test solution.

3.7.2 Raman Microscope Setup

As depicted in Figure 24, the Raman microscope was equipped with the epifluorescent microscope (BX61WI), Raman fiber probe sensor (SuperHead HE 640, Horiba Jobin Yvon), 632.8 nm HeNe Laser (LGK 7665 P18, LASOS) with the power of 5mW. The test sample was observed by the 20X objective lens (MPlanFLN, Olympus). Collected scattering light would pass through the long-pass filter, dispersed by an 80-cm spectrograph (1200 gr/mm), and finally detected by the CCD (354308, Horiba). The SERS spectrum was acquired by setting the 1 s integration time and 3 times the average spectrum in the NGSLabSpec software. Each sample would be randomly detected at the 3 positions with an interval of 60 μm . Before detection, the Raman microscope was calibrated by the silicon wafer, and the spectrometer was adjusted to 520.7 cm^{-1} .

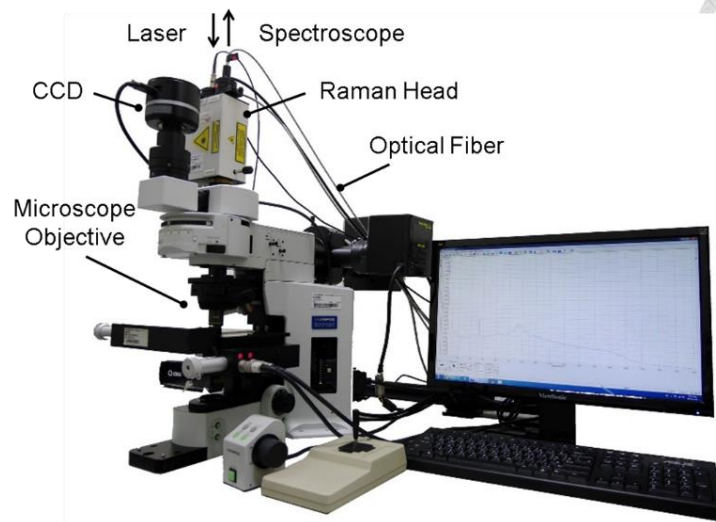


Figure 24 The Raman microscope. [36]

3.7.3 Data Processing

The acquired SERS spectrum data was processed baseline removal by the Python code which uses the sensitive nonlinear iterative peak clipping algorithm.

3.8 System Setup

The overall system is shown in Figure 25 and was connected by the pressure pump, microfluidic chip, and Raman microscope. To keep the water droplet confined in the microwell without volume loss and dislocation, the pressure pump was used to control the pressure in the Tygon tube between the chip and pump. Besides, the pressure pump could be feedback controlled by the flow sensor. Therefore, the relationship between flow rate and pressure could be established in time without any pressure loss issue. According to previous research, the droplet-like design of the microfluidic chip could save the most volume loss. [23] Thus, the purpose of expectation could be finished and finally combined with the Raman microscope. In this way, the Raman microscope could automatically read the SERS signal by the motorized stage and NGSLabSpec software while the pressure pump automatically supplied the impulse wave of flow rate rhythmically by the ESI

software. For research motivation, the SERS spectrum of a high-affinity compound could be expected to be dominant in the first well, and the SERS spectrum of a low-affinity compound could be expected to appear in the following well. Thus, our purpose could be achieved by removing the signal of the high-affinity compound and enhancing the signal of the low-affinity compound.

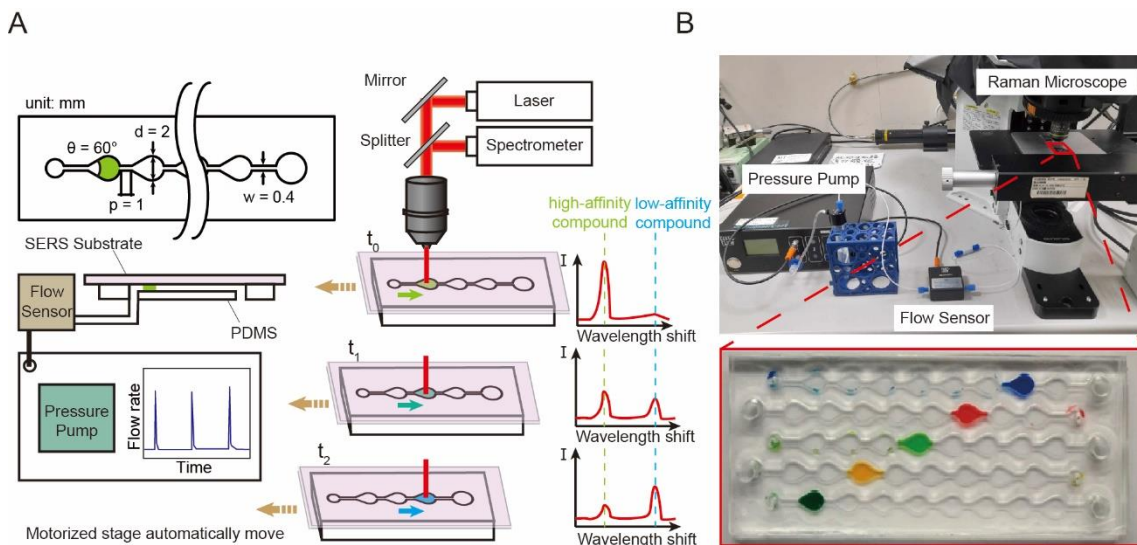


Figure 25 (A) System schematic of air-liquid microfluidic and Raman microscope. (B) The real image of the system schematic.

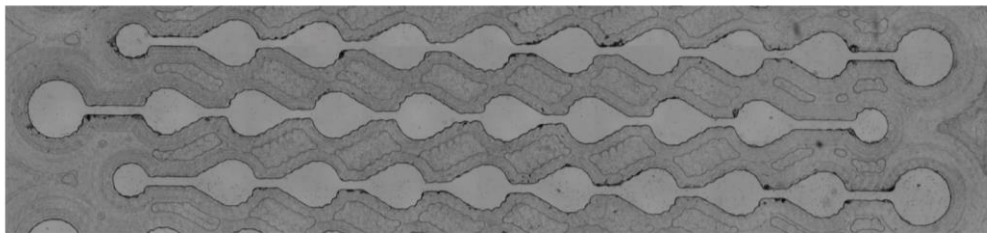
Chapter 4 Results and Discussion



4.1 Mold Fabrication

The PMMA mold was fabricated by the CNC machine. The results are shown in Figure 26. We found that the edge of the microfluidics was still rugged even when we used the 0.3 mm drill to mill the PMMA because of the limited spinning rate of 15000 rpm in Roland MDX-50. On the other hand, the edge of the microfluidic was smooth when the spinning rate of the drill reached 23000 rpm even when the 0.5 mm drill was used in Roland EGX-400. Therefore, the mold which was fabricated by Roland EGX-400 was used for the final version of microfluidics.

A



B

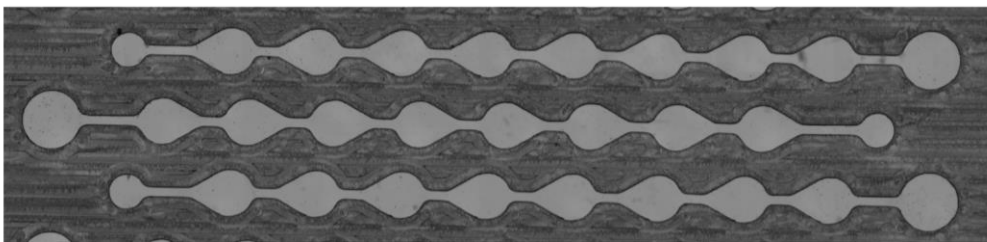


Figure 26 (A) The PMMA mold was fabricated by Roland MDX-50. (B) The PMMA mold was fabricated by Roland EGX-400.

4.2 Burst Pressure Experiment in Microfluidic Device

From the previous research, the burst pressure of the microfluidic device could be influenced by the channel width, channel height, contact angle between the air-liquid interface, and the surface tension between air and gas. To verify the hypothesis that the

smaller channel width needs to supply the larger pressure to drive the air-liquid microfluidics, different channel width designs with 0.5, 0.4, and 0.3 mm would be tested to observe the difference in the driving pressure in our pressure pumping system. The results are shown in Table 4. The theoretical number was calculated by the formula of the burst pressure with the contact angle of 112° and the surface tension of 0.054 N/m. We found that the difference between theoretical and experimental values is large, and the trends do not match. We suggest that the pressure the pressure pump supplied was already turned to the flow rate of liquid in our system. Therefore, the burst pressure no longer needs to be a concern in our system, on the other hand, the pressure we supply is larger than the previous reports because part of the pressure is used to squeeze the liquid in the Falcon tube.

Table 4 The driving pressure of the theoretical and experimental values.

Channel width (mm)	0.5	0.4	0.3
Theoretical (N/m ²)	148.34	168.57	202.28
Experimental (N/m ²)	5400	5100	4800

4.3 Optimization of Microfluidic Device Geometry

According to previous research and the theory of air-liquid interface, the channel height, width, and contact angle would influence the volume loss in microfluidics. [23] Although the previous research already told us that the wellhead of 60° had the best performance, we still need to confirm the situation in our case. Therefore, the microfluidics of different channel widths were first fabricated by the Roland MDX-50. The microfluidic chip was then attached to a glass slide, and the volume loss was estimated by using fluorescent Rhodamine 6G to count the area where the fluid remained

under the fluorescent microscope and then analyzed by ImageJ. The results are shown in Figure 27, we could find that the channel width of 0.4 mm would have the least volume loss. The analysis results are shown in Table 5 which is fulfilled by counting the area of each channel. It still had a 0.465 mm² of liquid that remained in microfluidic because of the nick of the PMMA mold.

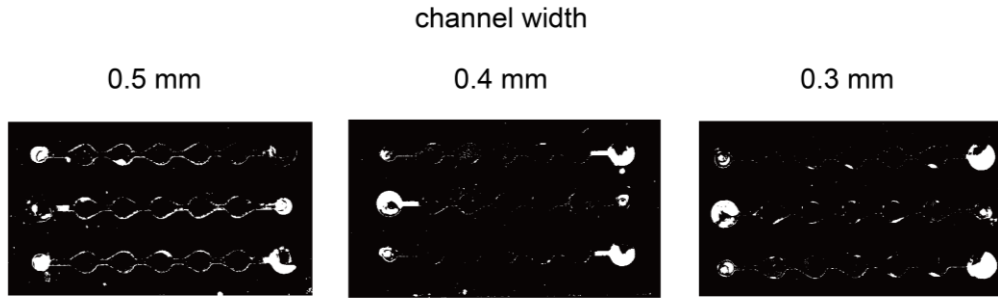


Figure 27 The fluorescent image of the microfluidic channel after the droplet moved.

Table 5 The volume loss analysis of different channel widths.

Channel width (mm)	0.5	0.4	0.3
Area (mm ²)	2.510	0.465	0.880
Standard deviation (mm ²)	0.321	0.174	0.255

Therefore, we further crafted the PMMA mold with the Roland EGX-400 and evaluated the volume loss again and the percentage of area that the droplet was in the well. We changed the fluorescent dye from Rhodamine 6G to Fluorescein isothiocyanate (FITC) because Rhodamine 6G would stick on the microfluidic channel. The results are shown in Figure 28 which connected the whole system on the fluorescent microscope as illustrated in Figure 29, we discovered that the droplet would be confined in the well with some degree of offset because of the difference of pressure recovery at every time before pushing. The analysis results are shown in Table 6, we found that the volume ratio would maintain above 70%. Although the droplet would confine perfectly in well 2, the

percentage would not go to 100% because of the different amounts that are lost at the inlet. We set the area confined in well 2 as 100%, and the volume confined in the well would maintain above 90%

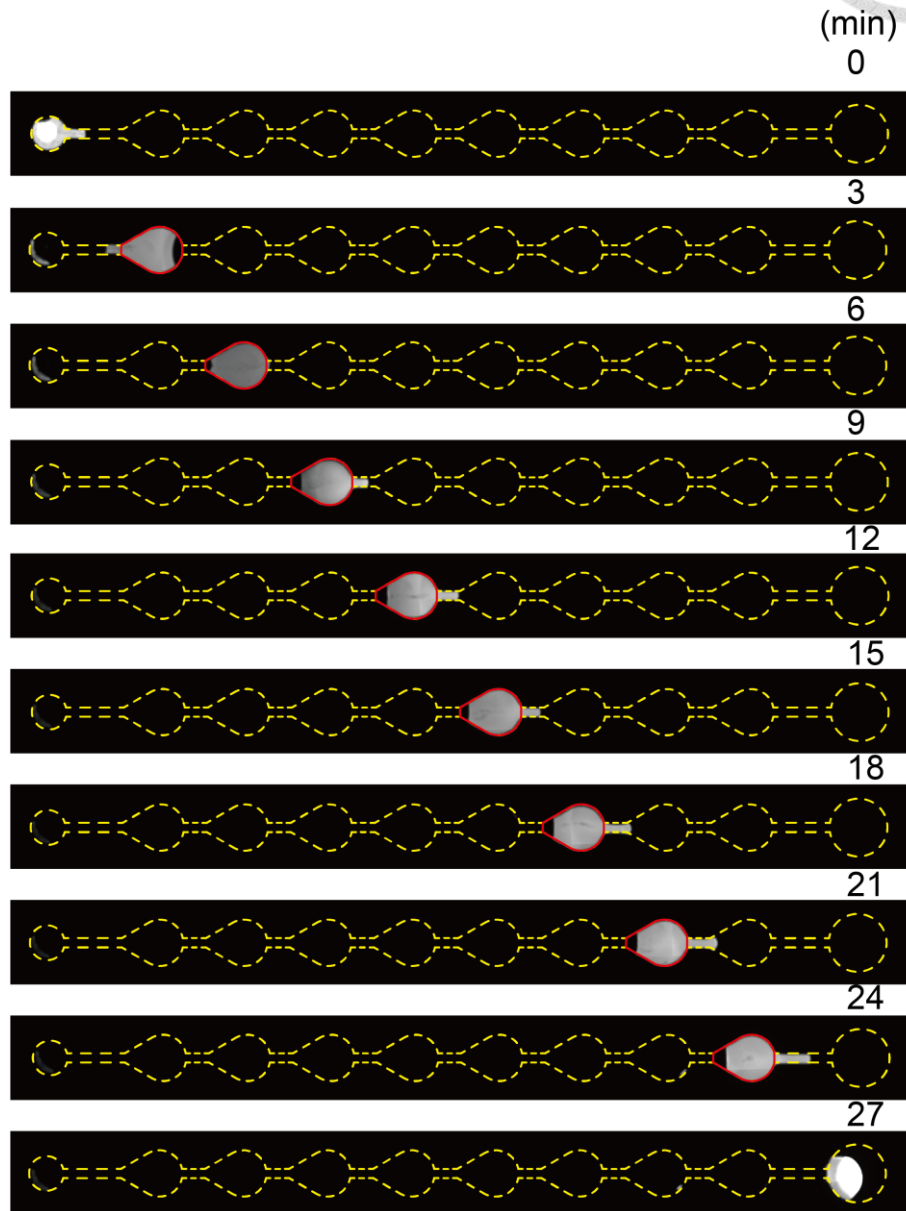
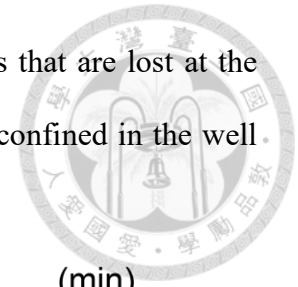


Figure 28 The air-liquid microfluidics performance under the fluorescent microscope.

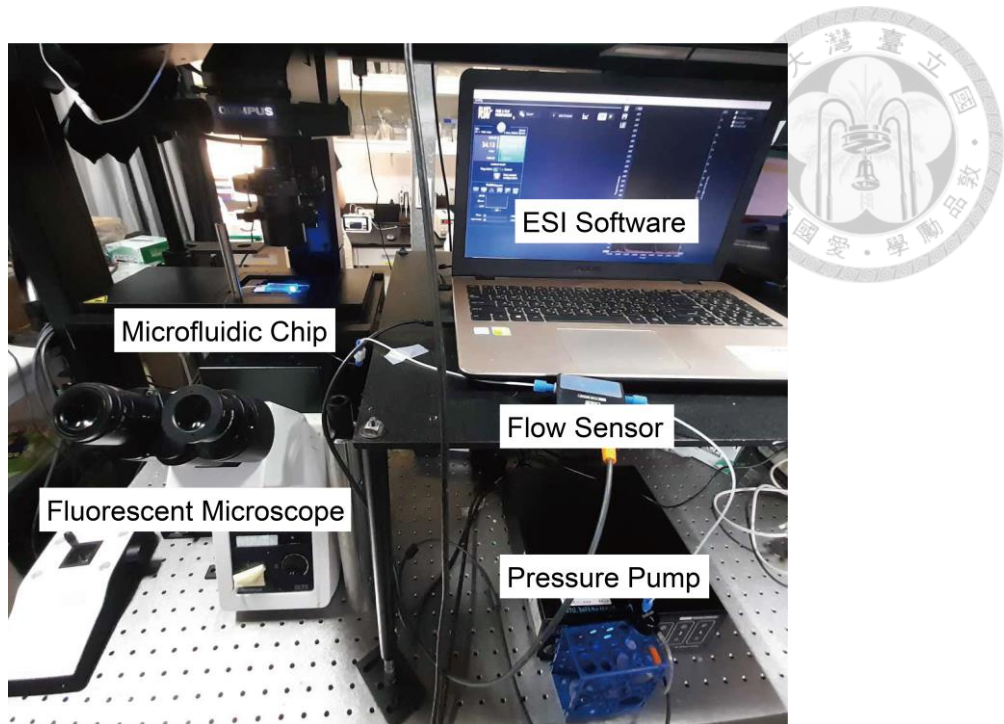


Figure 29 The setup of the pressure pumping system and fluorescent microscope.

Table 6 The surface area analysis at different wells.

	Surface area (mm ²)	Volume ratio (%)	Relative volume ratio (%)
Well 1	3.23	75	91
Well 2	3.50	82	100
Well 3	3.22	75	91
Well 4	3.26	76	93
Well 5	3.31	77	94
Well 6	3.15	73	89
Well 7	3.14	73	89
Well 8	3.21	75	91

4.4 Adsorption of Single Analyte

4.4.1 Adsorption Time Evaluation



Before applying our microfluidic system, the adsorption time needed to be decided to confirm that the reaction was completed. The research investigated the reaction time between the high-affinity analyte and the deposition-made substrate. They found that the SERS signal became saturated after 60 seconds. [34] Based on this research, we dropped a 2.5 mL droplet of adenine on the SERS substrate for 1, 3, and 5 minutes and pipetted it into another position on the SERS substrate, which is illustrated in Figure 30A. The results are shown in Figure 30B-D, we could obviously see the characteristic peak of adenine at 733 cm^{-1} which came from the signal of the symmetric ring breathing mode would decrease to some degree. The rough results finished by the pipetting would have some issues with the irregularity of the adsorbing surface and the evaporation effect from the air. To precisely confirm the results shown in Figure 30, we introduce adenine in our microfluidic system. Our microfluidic chip was made by combining the PDMS channel and SERS substrate as illustrated in Figure 31A. The fabrication method was vacuum heating the PDMS film which is made by spin coating and packaged by vacuum package machine as illustrated in Figure 31B. The microfluidic chip was then inversely placed on the Raman microscope and connected to the pressure pumping system which is shown in Figure 31C, D, and E. Compared with the adenine in microfluidics, the adsorbing surface in the pipetting method was larger than in the microfluidic method, causing the attenuation curve of 1 minute that sharper than microfluidic method. Because of the evaporation effect, the attenuation curve of 1 and 3 minutes would have different situations in the pipetting method and microfluidic method. Both data from the pipetting method and the microfluidic method of 5 minutes would have the problem of over-

absorbing. Therefore, the adsorbing time of 3 minutes was chosen which is linear and the number of wells would increase to 8 in order to see the complete adsorption of adenine solution.

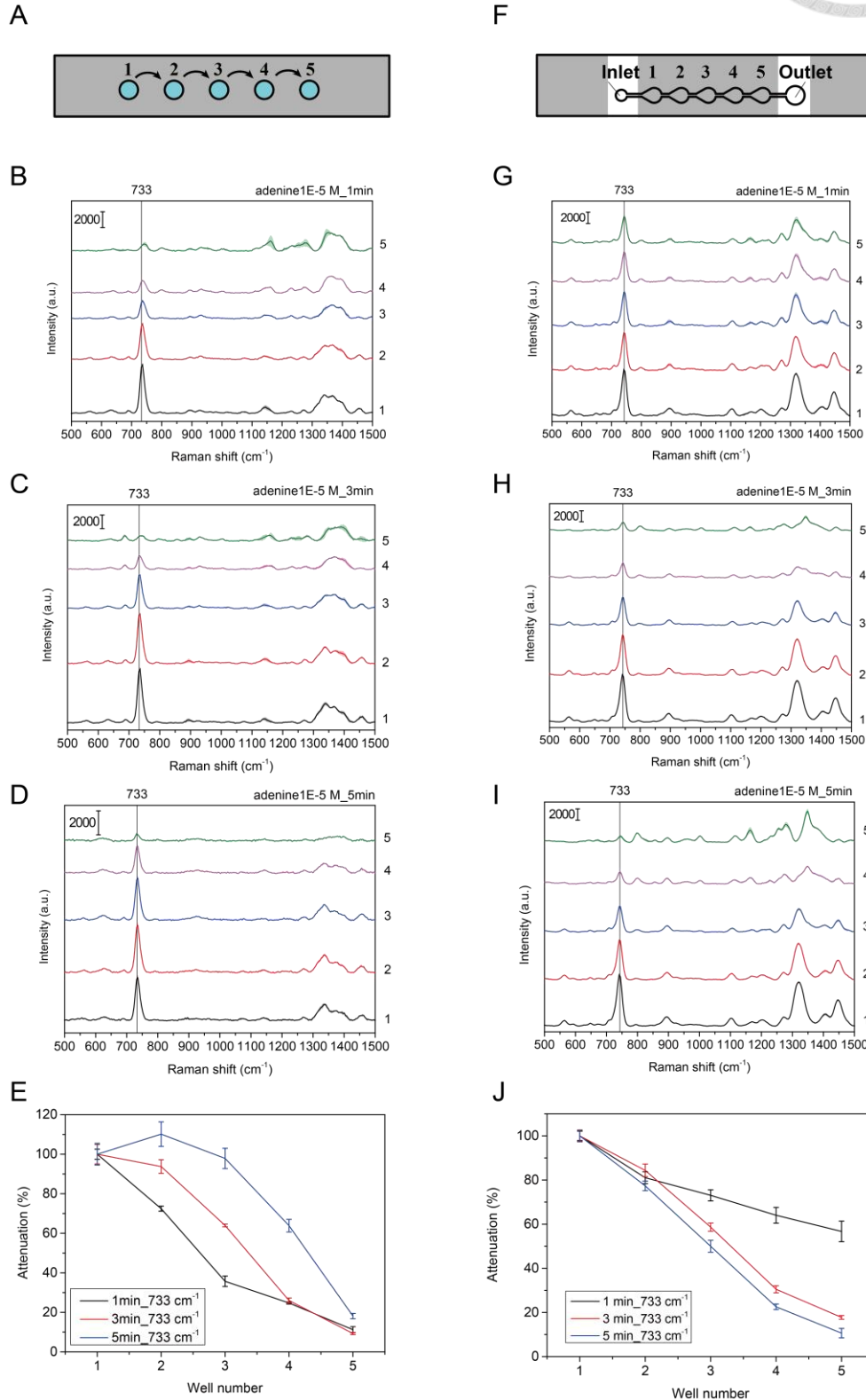
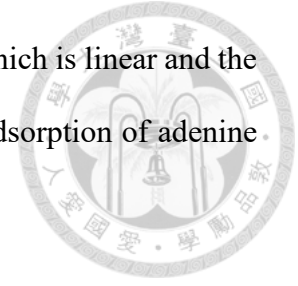


Figure 30 (A) Schematic of SERS detection by pipette. The SERS spectrum of 10^{-5} M adenine in different positions with adsorption time of (B) 1 min (C) 3 min (D) 5 min. (E) The attenuation of the SERS signal at 733 cm^{-1} under different adsorption times (1, 3, and 5 minutes). (F) Schematic of SERS detection by the pumping system. SERS spectrum of 10^{-5} M adenine in different wells with adsorption time of (G) 1 min (H) 3 min (I) 5 min. (J) The attenuation of the SERS signal at 733 cm^{-1} under different adsorption times in the pumping system (1, 3, and 5 minutes).

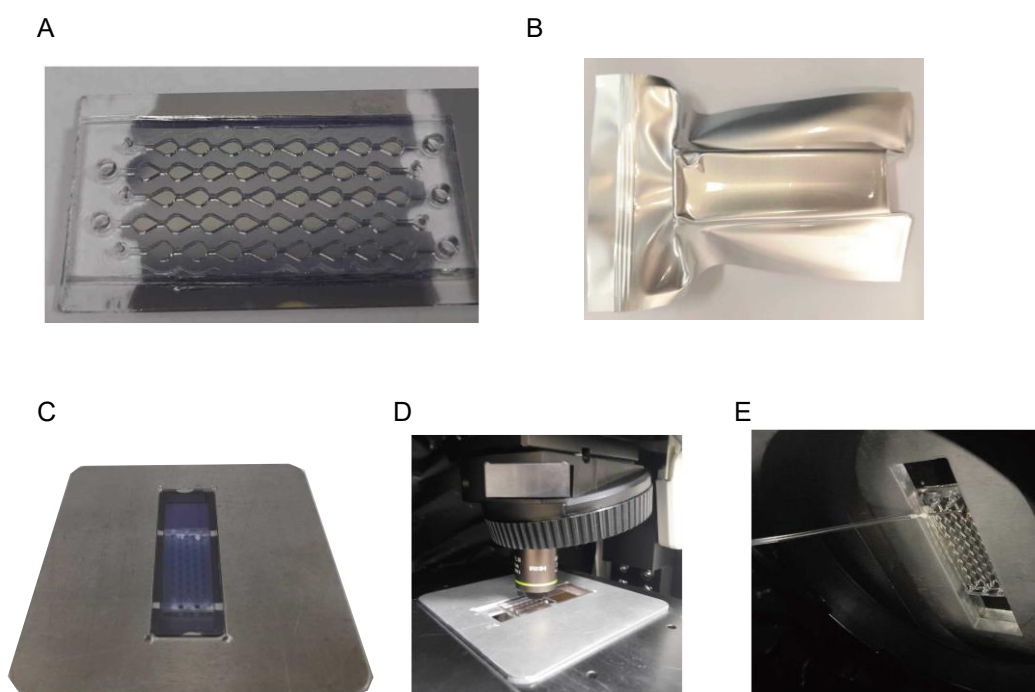
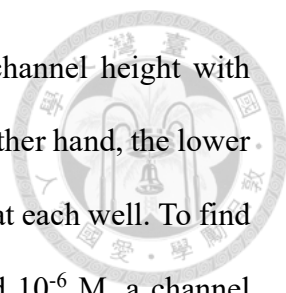


Figure 31 (A) The combination of PDMS channel and SERS substrate. (B) The image of the microfluidic chip in the chip mailer and vacuumed by the package machine. (C) The microfluidic chip invert is placed on the mold of the motorized stage. (D) The Raman microscope and our microfluidic chip. (E) The microfluidic chip is connected to a pressure pump under the Raman microscope.

4.4.2 Channel Height Evaluation

After deciding 3 minutes adsorption time and increasing the number of wells to 8, another parameter that may affect the SERS signal is the height of the channel of the



microfluidics. Because of the volume-to-surface ratio, the higher channel height with large amounts of adenine would slowly adsorb in each well. On the other hand, the lower channel height with small amounts of adenine would adsorb quickly at each well. To find an appropriate range of adenine concentrations between 10^{-5} M and 10^{-6} M, a channel height of 150 to 600 μm was designed. The results are shown in Figure 32, we could observe that the signal at 733 cm^{-1} which represents the signal of adenine would disappear in different well numbers at different channel heights. With the channel height of 600 μm , the 10^{-5} M adenine cannot be adsorbed completely. We can still see a peak at 733 cm^{-1} . On the other hand, 10^{-5} M adenine would quickly be adsorbed with a channel height of 150 μm , making it difficult to observe the dynamic behavior. Therefore, the microfluidic device with a channel height of 300 μm was chosen for the further experiment because it could fit the adenine range appropriately. Besides, the reason why not choosing the design of the channel height of 150 μm by decreasing the adsorption time to observe the dynamic behavior is that the pressure pump makes it hard to control the droplet less than 1 μL which is the droplet volume in the design of the channel height of 150 μm .

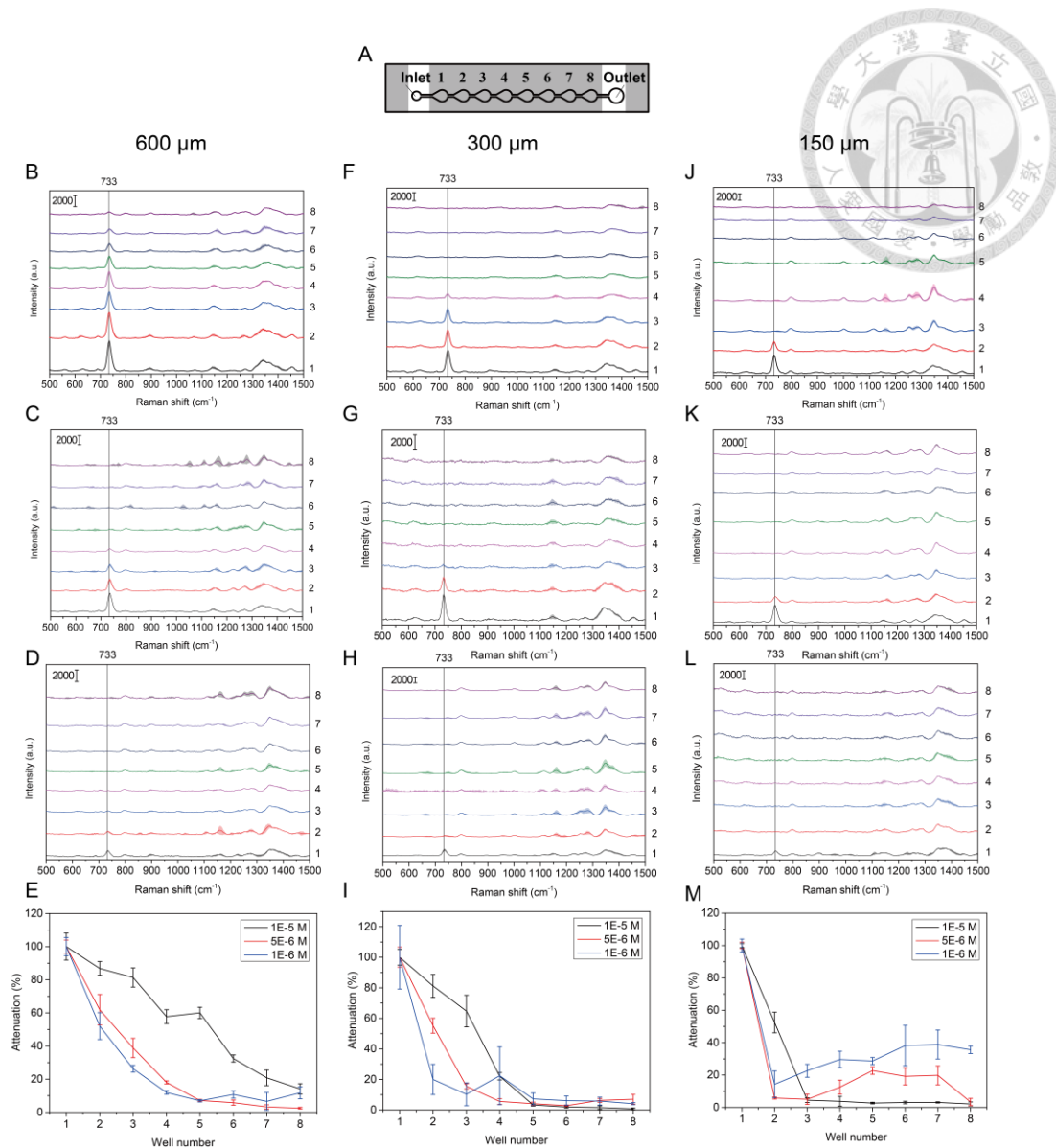
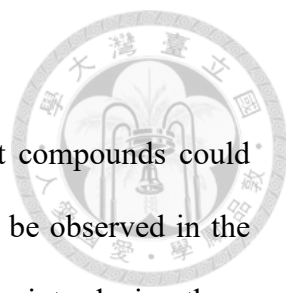


Figure 32 (A) Schematic of SERS detection by the pumping system with the adsorption time of 3 minutes. The SERS spectrum of (B) 10^{-5} M (C) 5×10^{-6} M (D) 10^{-6} M adenine in different wells with a channel height of $600 \mu\text{m}$. (E) The attenuation curve at 733 cm^{-1} with a channel height of $600 \mu\text{m}$. The SERS spectrum of (F) 10^{-5} M (G) 5×10^{-6} M (H) 10^{-6} M adenine in different wells with a channel height of $300 \mu\text{m}$. (I) The attenuation curve at 733 cm^{-1} with a channel height of $300 \mu\text{m}$. The SERS spectrum of (J) 10^{-5} M (K) 5×10^{-6} M (L) 10^{-6} M adenine in different wells with a channel height of $150 \mu\text{m}$. (M) The attenuation curve at 733 cm^{-1} with a channel height of $150 \mu\text{m}$.

4.4.3 Adsorption with Different Compounds



Once the channel height was determined at 300 μm , different compounds could appear in the bacterial supernatant or other biomolecules that could be observed in the SERS spectrum, including uracil, cytosine, hypoxanthine, etc. Before introducing these kinds of compounds, the linear range of different compounds needs to be observed to prevent the misunderstanding of the attenuation curve. The dynamic range of the common purine derivatives is shown in Figure 33. The dynamic range of guanine is between 10^{-4} and 10^{-5} M, hypoxanthine is between 10^{-4} and 10^{-8} M, and adenine is between 10^{-5} and 10^{-8} M. For those compounds with pyrimidine based, including cytosine, thymine, and uracil, the dynamic range is between 10^{-3} and 5×10^{-6} M. After confirming the dynamic range, we introduced these purine derivatives into the air-liquid microfluidics. The results are shown in Figure 34. For guanine, hypoxanthine, cytosine, thymine, and uracil, the breathing mode of the ring at 660, 740, 796, 780, and 800 cm^{-1} , respectively, is very strong in SERS. We depicted it as the signal of analyte and found that adenine, hypoxanthine, and thymine have a high affinity with silver SERS substrate. On the other hand, cytosine, and guanine have low affinity with silver SERS substrate. Although there are still some issues that the concentration would influence the attenuation curve, we could separate the high-affinity compound and low-affinity compound by observing the intensity of after microfluidic to before microfluidic ratio. For example, the attenuation ratio of adenine, hypoxanthine, and guanine is 0.8, 4.6, and 1.7%, respectively, serving as the high-affinity compounds. The attenuation ratio of uracil, cytosine, and thymine is 112, 95, and 90%, respectively, serving as low-affinity compounds with some deviation in the detection.

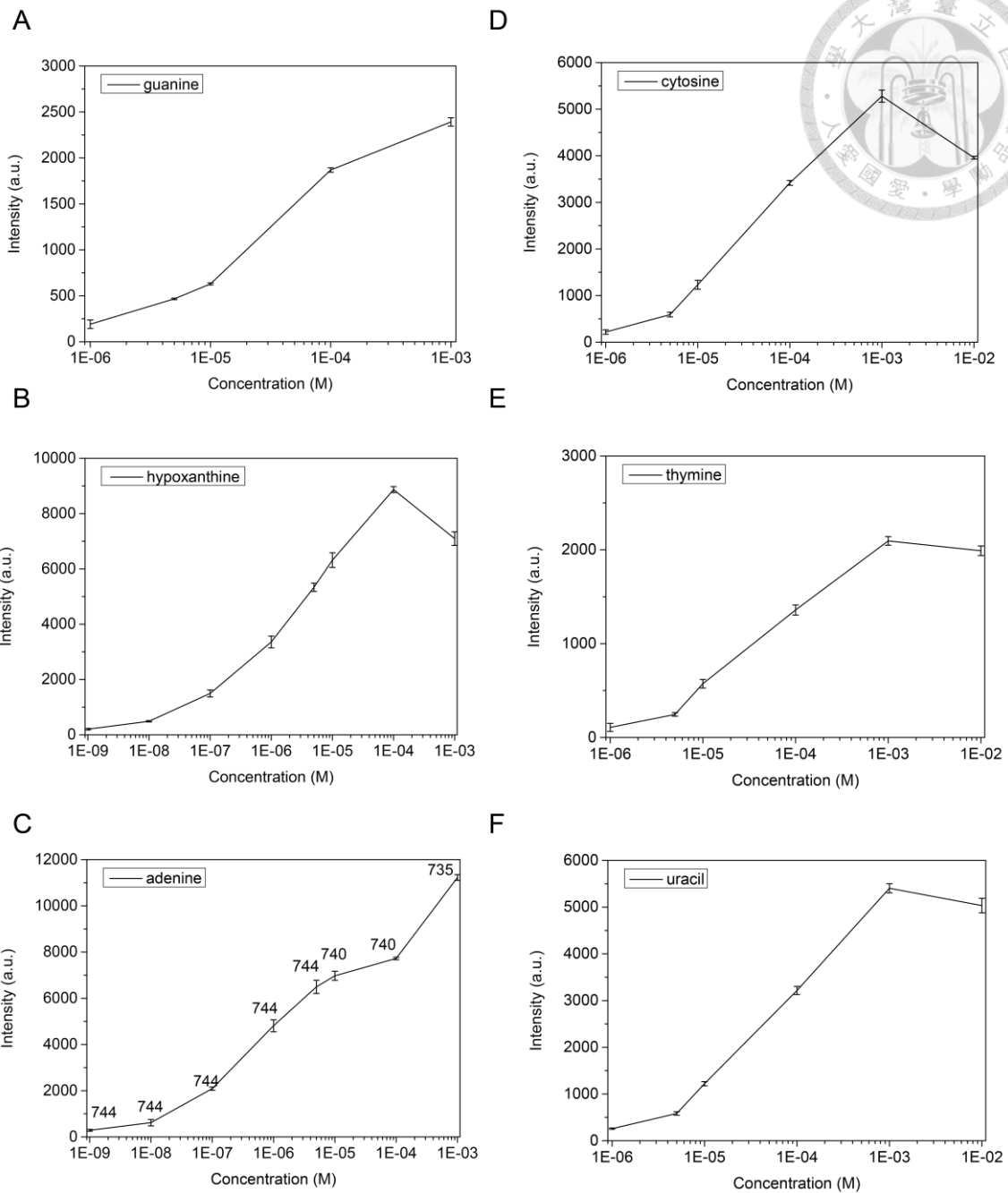


Figure 33 The dynamic range of the (A) guanine (B) hypoxanthine (C) adenine (D) cytosine (E) thymine (F) uracil in the SERS detection method.

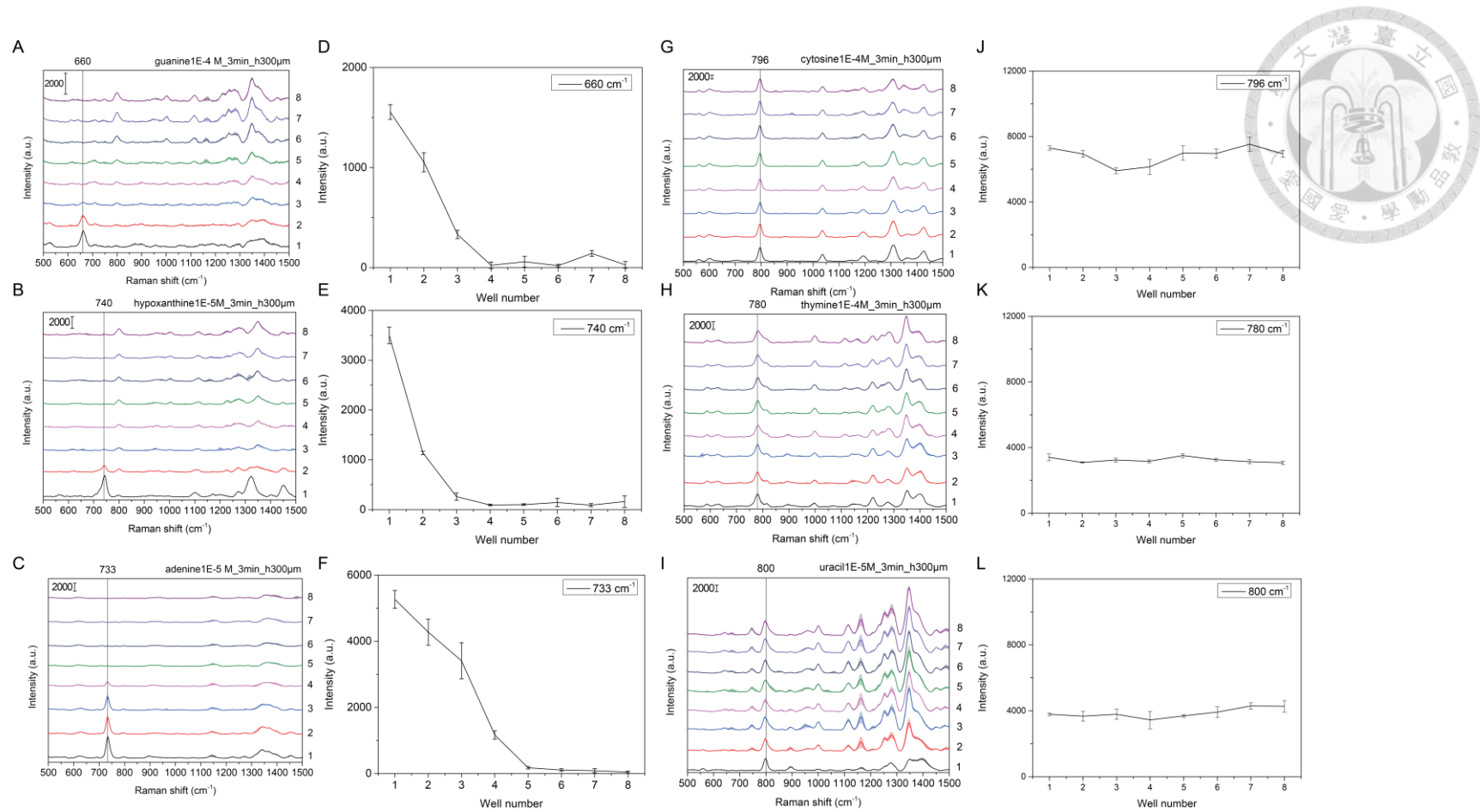
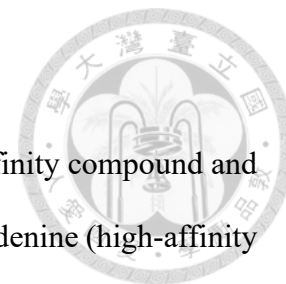


Figure 34 The SERS spectrum of (A) 10^{-4} M guanine (B) 10^{-5} M hypoxanthine (C) 10^{-5} M adenine (G) 10^{-4} M cytosine (H) 10^{-4} M thymine (I) 10^{-5} M uracil in our microfluidic system (3 minutes adsorption time and 300 μm channel height). The attenuation of the SERS signal at (D) 660 cm^{-1} (E) 740 cm^{-1} (F) 733 cm^{-1} (J) 796 cm^{-1} (K) 780 cm^{-1} (L) 800 cm^{-1} .

4.5 Competitive Adsorption of Two Analytes



To prove that our microfluidic system could adsorb the high-affinity compound and enhance the signal of the low-affinity compound, different ratios of adenine (high-affinity compound) and uracil (low-affinity compound) solution were mixed for proof of concept. The results are shown in Figure 35. At the 10:1 adenine to uracil ratio, we could observe that the adenine signal could block the uracil signal because of affinity in Figure 35A. However, the signal of uracil came out at the back well after the adsorption of our microfluidics. Moreover, different ratios of the adenine and uracil mix solutions would have different patterns of attenuation lines as illustrated in Figure 35F-J, showing that they are different even though the initial condition appeared the same in the SERS spectrum.

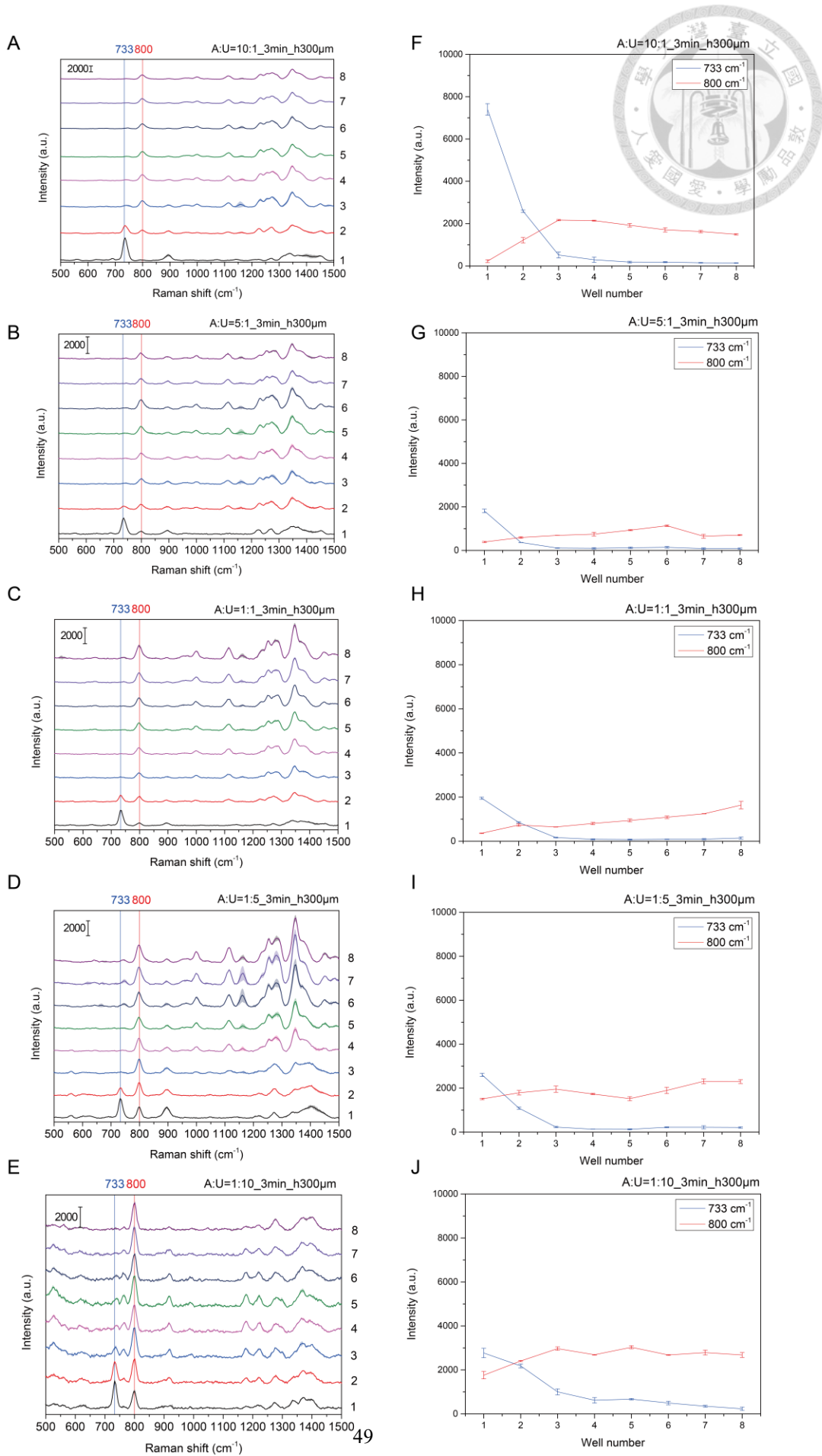
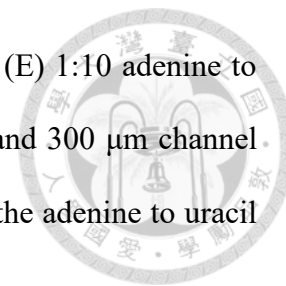


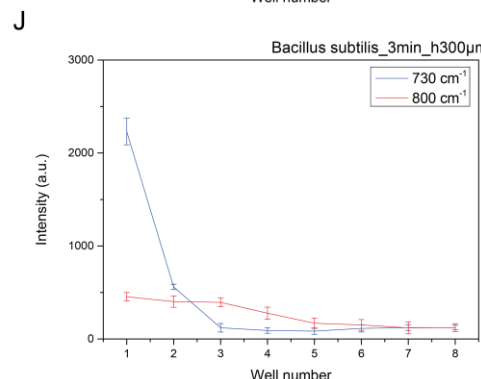
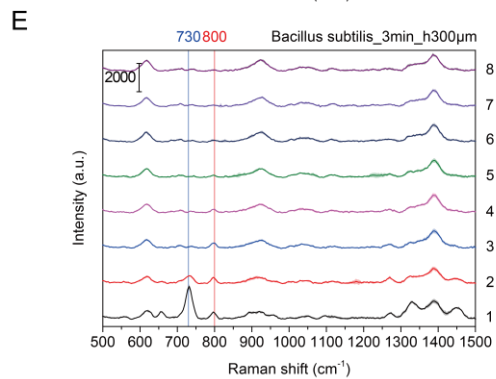
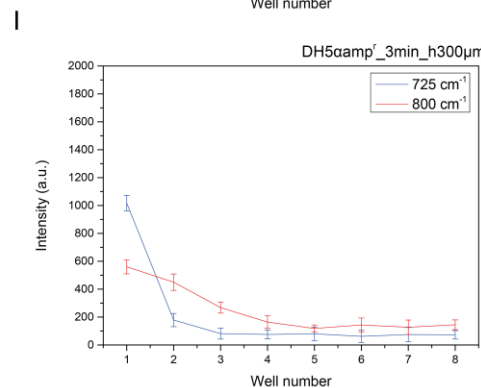
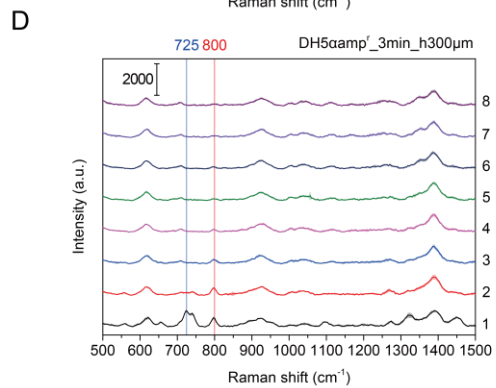
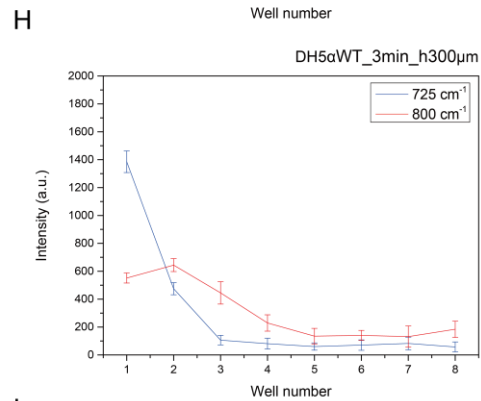
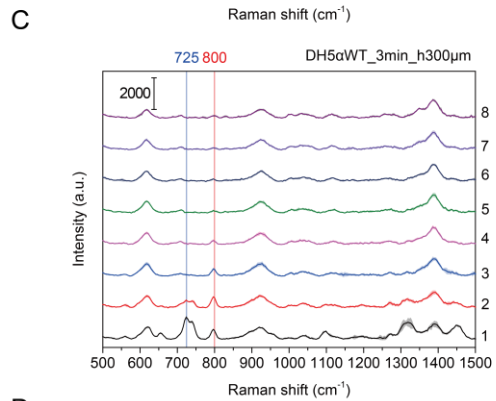
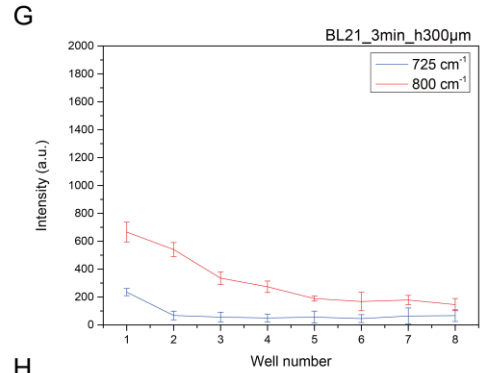
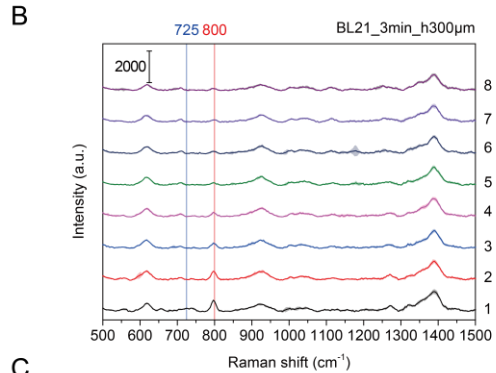
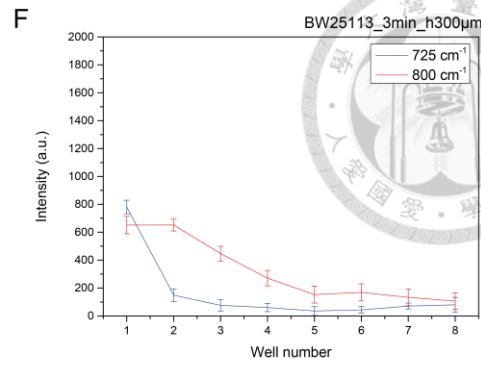
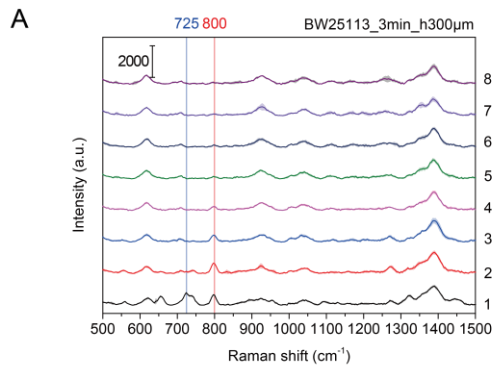
Figure 35 The SERS spectrum of (A) 10:1 (B) 5:1 (C) 1:1 (D) 1:5 (E) 1:10 adenine to uracil ratio in our microfluidic system (3 minutes adsorption time and 300 μm channel height). The attenuation of the SERS signal at 733 and 800 cm^{-1} in the adenine to uracil ratio of (F) 10:1 (G) 5:1 (H) 1:1 (I) 1:5 (J) 1:10.



4.6 Bacteria Identification by Microfluidic Device

After proving that our microfluidic system could separate the different adsorptive compounds by the SERS substrate, the unmet needs still need to be solved when it comes to real samples. Because rapid identification of bacteria is important in sepsis or other infections caused by bacteria, growth-free and low detection time is the condition we need to achieve. The bacterial supernatant composed of different purine derivatives could identify the bacteria because different kinds of bacteria would have different pathways and enzymes. Moreover, the bacterial supernatant could be gained in 30 minutes. Therefore, bacterial supernatant is our target sample in our microfluidic system.

By introducing the bacterial supernatant of the *E. coli* strain with the negative control of gram-positive bacteria, *B. subtilis*, into our microfluidic system, the results are shown in Figure 36. The SERS signal of different *E. coli* supernatants would show a similar spectrum at the beginning and the end, but different during the measurement. That is because different kinds of compounds would be adsorbed by SERS substrate in some ratio of composition. Finally, all compounds would be adsorbed totally at the end of the well, causing the same spectrum. By analyzing the attenuation at each Raman shift shown in Figure 36 F-J, the differences in bacterial supernatant could be identified even in the bacteria whether in the resistant strain.



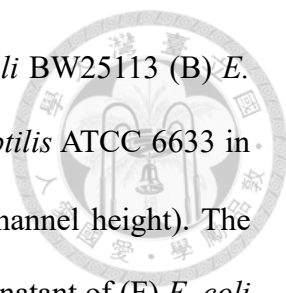


Figure 36 The SERS spectrum of bacterial supernatant of (A) *E. coli* BW25113 (B) *E. coli* BL21 (C) *E. coli* DH5 α WT (D) *E. coli* DH5 α Amp^r (E) *B. subtilis* ATCC 6633 in our microfluidic system (3 minutes adsorption time and 300 μ m channel height). The attenuation of SERS signal at 725 and 800 cm^{-1} in the bacterial supernatant of (F) *E. coli* BW25113 (G) *E. coli* BL21 (H) *E. coli* DH5 α WT (I) *E. coli* DH5 α Amp^r (J) *B. subtilis* ATCC 6633.

4.7 Principal Component Analysis (PCA)

Principal component analysis (PCA), is a distant-based ordination technique used to display the patterns in multivariate data. It is used to reduce the multi-dimensional data to a lower dimension for further analysis. In PCA, the new variables are called principal components (PCs) which is the linear combination of the real variables, and the first component is the greatest amount of variation. The points in the plot represent the new position in the scale of PC of each sample, therefore, the similar samples would cluster together. When we conduct the PCA for the SERS spectrum of bacterial supernatant from Figure 36, the results are shown in Figure 37. we could find that the *E. coli* bacteria with the strain of DH5 α wildtype and ampicillin resistance would overlap together without using the air-liquid microfluidics. Also, it becomes more divided from each cluster by using our microfluidic system, showing that our microfluidic system is better than the traditional method.

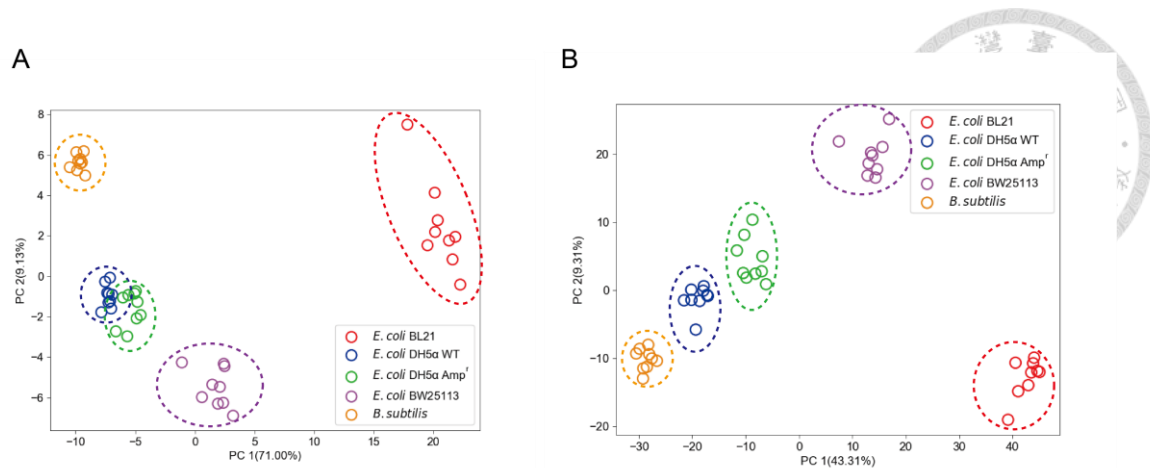


Figure 37 (A) The PCA of the only well 1 data in each sample (N=9). (B) The PCA of combining well 1 to well 8 data in each sample (N=9).

4.8 Machine Learning Method of Supporting Vector Machine (SVM)

Supporting vector machine (SVM) is one of the machine learning methods based on the results of PCA. It is a supervised learning algorithm to find an optimal hyperplane that can separate each class of the sample, and we call this hyperplane a decision boundary. In SVM, we used a one-vs-rest classifier for multi-class classification, randomly splitting the dataset with a ratio of 7:3 for machine learning. Before using the air-liquid microfluidic channel, the accuracy was only 95%. The prediction errors occurred in data involving resistant and non-resistant samples. However, after using the channel, the accuracy reached 100%, showing enhanced discrimination capability.

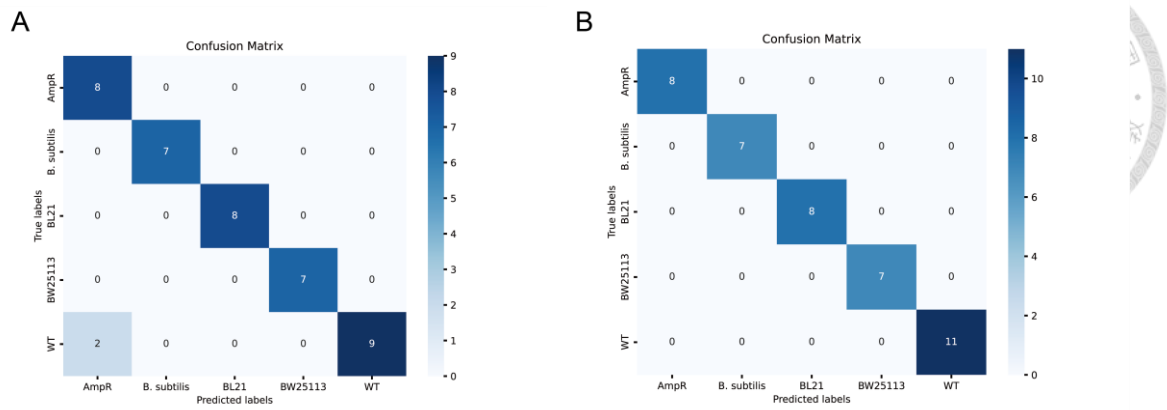
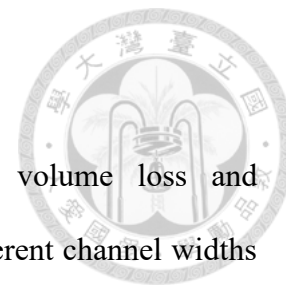


Figure 38 (A) The confusion matrix of SVM with only well 1 data in each sample (N=27).
 (B) The confusion matrix of SVM with combining well 1 to well 8 data in each sample (N=27).

Chapter 5 Conclusions



In conclusion, using air-liquid microfluidics can reduce volume loss and automatically control the droplet position in the microfluidics. Different channel widths of microfluidic would cause different volume loss. We found the best channel width of 0.4 mm and tested the adenine solution which is usually in the bacterial supernatant. The adsorption time of 3 minutes could fulfill the reaction between the adenine and the SERS substrate. Also, we found the height of the 300 μm microfluidic channel was suitable for observing the attenuation of the 10^{-5} to 10^{-6} M concentration of adenine solution. By applying our microfluidic system to different kinds of biomolecules, such as uracil, cytosine, thymine, and hypoxanthine, we could define the high-affinity compound and low-affinity compound to the SERS substrate. Our microfluidic platform verifies our hypothesis that adsorb the high-affinity compound and enhances the signal of the low-affinity compound by mixing with different ratios of adenine and uracil solution. Finally, this system also could separate the complex composition solution such as bacterial supernatant. By the conception of adsorptive separation, different compositions of two kinds or more would have a different pattern of attenuation curve, showing the ability of bacteria identification. In PCA, the different bacterial supernatants could be more separated from each cluster, showing the high performance of bacteria identification. In SVM, we showed that air-liquid microfluidics really can help bacteria identification in the machine learning method by expanding the data inside the single droplet.

Chapter 6 Future Work



In this thesis, we demonstrate the air-liquid microfluidic can control the droplet position without volume loss and dislocation. Also, the automatic On-chip SERS detection could be achieved by the pumping system and motorized stage. Finally, showing the ability of bacteria identification than the traditional methods. But there are some problems that still need to be solved for further application and investigation.

(1) The Enhanced Signal of a Single Low-affinity Compound

As illustrated in Figure 34, the attenuation curve of uracil, cytosine, and thymine would go up in the SERS spectrum. The reason for this phenomenon is the silver nanoparticles would be moved downstream of microfluidics, thus enhancing the SERS signal. To drive this kind of problem, there are two kinds of solutions to solve this problem. The first is to increase the bonding between glass slides and silver nanoparticles. Another is to use the SERS substrate made by the electroplating on the AAO.

(2) Machine Learning to Evaluate the Performance by Using Air-liquid Microfluidics

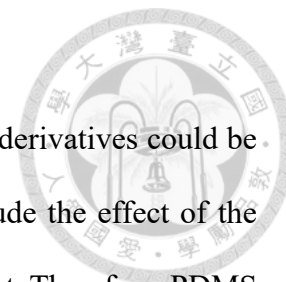
Our microfluidic device could generate the detail in the single droplet solution. The advantage of the microfluidic system could appear in the simple machine learning method, which could be easily explained. Once the reproducibility can be ensured, a large sample is still needed to do the machine learning.

(3) Verification of the composition of the bacterial supernatant

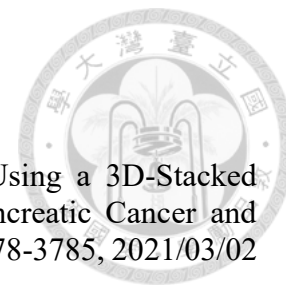
Based on the research hypothesis, the air-liquid microfluidics utilize the composition difference in bacterial supernatant to identify the bacteria. Therefore, high-performance liquid chromatography (HPLC) analysis is needed to prove that the reconstituted solution from the HPLC results will be similar to the obtained bacterial supernatant.

(4) Evidence that PDMS does not adsorb purine derivatives

Although we have already proven that the high-affinity purine derivatives could be adsorbed by the silver SERS active substrate. We still do not exclude the effect of the PDMS adsorption or prove that it is not an influence in our experiment. Therefore, PDMS modification with Teflon needs to be tested for the different kinds of components including the fluorescent molecules that exhibit adsorption reactions with PDMS like Rhodamine 6G.



REFERENCE



- [1] J. B. Phyto *et al.*, "Label-Free SERS Analysis of Urine Using a 3D-Stacked AgNW-Glass Fiber Filter Sensor for the Diagnosis of Pancreatic Cancer and Prostate Cancer," *Analytical Chemistry*, vol. 93, no. 8, pp. 3778-3785, 2021/03/02 2021, doi: 10.1021/acs.analchem.0c04200.
- [2] W. Wang, S. Kang, and P. J. Vikesland, "Surface-Enhanced Raman Spectroscopy of Bacterial Metabolites for Bacterial Growth Monitoring and Diagnosis of Viral Infection," *Environmental Science & Technology*, vol. 55, no. 13, pp. 9119-9128, 2021/07/06 2021, doi: 10.1021/acs.est.1c02552.
- [3] A. Haddad, M. A. Comanescu, O. Green, T. A. Kubic, and J. R. Lombardi, "Detection and Quantitation of Trace Fentanyl in Heroin by Surface-Enhanced Raman Spectroscopy," *Analytical Chemistry*, vol. 90, no. 21, pp. 12678-12685, 2018/11/06 2018, doi: 10.1021/acs.analchem.8b02909.
- [4] L. He, T. Chen, and T. P. Labuza, "Recovery and quantitative detection of thiabendazole on apples using a surface swab capture method followed by surface-enhanced Raman spectroscopy," *Food Chemistry*, vol. 148, pp. 42-46, 2014/04/01/ 2014, doi: <https://doi.org/10.1016/j.foodchem.2013.10.023>.
- [5] N. Choi *et al.*, "Integrated SERS-Based Microdroplet Platform for the Automated Immunoassay of F1 Antigens in *Yersinia pestis*," *Analytical Chemistry*, vol. 89, no. 16, pp. 8413-8420, 2017/08/15 2017, doi: 10.1021/acs.analchem.7b01822.
- [6] S. Azimi and A. Docoslis, "LESS is more: Achieving sensitive protein detection by combining electric field effects and surface-enhanced Raman scattering," *Sensors and Actuators B: Chemical*, vol. 393, p. 134250, 2023/10/15/ 2023, doi: <https://doi.org/10.1016/j.snb.2023.134250>.
- [7] R. Panneerselvam, H. Sadat, E.-M. Höhn, A. K. Das, H. Noothalapati, and D. Belder, "Microfluidics and surface-enhanced Raman spectroscopy, a win-win combination?," *Lab on a chip*, 2022.
- [8] M. Becker, C. Budich, V. Deckert, and D. Janasek, "Isotachophoretic free-flow electrophoretic focusing and SERS detection of myoglobin inside a miniaturized device," *Analyst*, 10.1039/B816717F vol. 134, no. 1, pp. 38-40, 2009, doi: 10.1039/B816717F.
- [9] W. R. Premasiri, J. C. Lee, A. Sauer-Budge, R. Théberge, C. E. Costello, and L. D. Ziegler, "The biochemical origins of the surface-enhanced Raman spectra of bacteria: a metabolomics profiling by SERS," *Analytical and Bioanalytical Chemistry*, vol. 408, no. 17, pp. 4631-4647, 2016/07/01 2016, doi: 10.1007/s00216-016-9540-x.
- [10] B. Krafft, A. Tycova, R. D. Urban, C. Dusny, and D. Belder, "Microfluidic device for concentration and SERS-based detection of bacteria in drinking water," *ELECTROPHORESIS*, vol. 42, no. 1-2, pp. 86-94, 2021/01/01 2021, doi: <https://doi.org/10.1002/elps.202000048>.
- [11] A. Walter, A. März, W. Schumacher, P. Rösch, and J. Popp, "Towards a fast, high specific and reliable discrimination of bacteria on strain level by means of SERS in a microfluidic device," *Lab on a Chip*, 10.1039/C0LC00536C vol. 11, no. 6, pp. 1013-1021, 2011, doi: 10.1039/C0LC00536C.
- [12] J. Zhuang *et al.*, "SERS-based CRISPR/Cas assay on microfluidic paper analytical devices for supersensitive detection of pathogenic bacteria in foods," *Biosensors and Bioelectronics*, vol. 207, p. 114167, 2022/07/01/ 2022, doi:

- <https://doi.org/10.1016/j.bios.2022.114167>.
- [13] K.-W. Chang, H.-W. Cheng, J. Shiue, J.-K. Wang, Y.-L. Wang, and N.-T. Huang, "Antibiotic Susceptibility Test with Surface-Enhanced Raman Scattering in a Microfluidic System," *Analytical Chemistry*, vol. 91, no. 17, pp. 10988-10995, 2019/09/03 2019, doi: 10.1021/acs.analchem.9b01027.
- [14] C. C. Liao, H. K. Huang, Y. Z. Chen, and N. T. Huang, "The Microfluidic Microwell Device Integrating Surface Enhanced Raman Scattering for Bacteria Enrichment and in Situ Antibiotic Susceptibility Test," in *2020 IEEE 33rd International Conference on Micro Electro Mechanical Systems (MEMS)*, 18-22 Jan. 2020 2020, pp. 1048-1051, doi: 10.1109/MEMS46641.2020.9056435.
- [15] S.-J. Lin *et al.*, "An antibiotic concentration gradient microfluidic device integrating surface-enhanced Raman spectroscopy for multiplex antimicrobial susceptibility testing," *Lab on a Chip*, 10.1039/D2LC00012A vol. 22, no. 9, pp. 1805-1814, 2022, doi: 10.1039/D2LC00012A.
- [16] A. Mühlig *et al.*, "LOC-SERS: A Promising Closed System for the Identification of Mycobacteria," *Analytical Chemistry*, vol. 88, no. 16, pp. 7998-8004, 2016/08/16 2016, doi: 10.1021/acs.analchem.6b01152.
- [17] Y. Liu, G. Su, W. Wang, H. Wei, and L. Dang, "A novel multifunctional SERS microfluidic sensor based on ZnO/Ag nanoflower arrays for label-free ultrasensitive detection of bacteria," *Analytical Methods*, 10.1039/D4AY00018H 2024, doi: 10.1039/D4AY00018H.
- [18] H. Hong, J. M. Song, and E. Yeom, "Quantitative study for control of air-liquid segmented flow in a 3D-printed chip using a vacuum-driven system," *Scientific Reports*, vol. 12, no. 1, p. 8986, 2022/05/28 2022, doi: 10.1038/s41598-022-13165-6.
- [19] Y. Song, M. Baudoin, P. Manneville, and C. N. Baroud, "The air-liquid flow in a microfluidic airway tree," *Medical Engineering & Physics*, vol. 33, no. 7, pp. 849-856, 2011/09/01/ 2011, doi: <https://doi.org/10.1016/j.medengphy.2010.10.001>.
- [20] D. Huh *et al.*, "Use of Air-Liquid Two-Phase Flow in Hydrophobic Microfluidic Channels for Disposable Flow Cytometers," *Biomedical Microdevices*, vol. 4, no. 2, pp. 141-149, 2002/05/01 2002, doi: 10.1023/A:1014691416614.
- [21] Y. Kazoe, T. Matsuno, I. Yamashiro, K. Mawatari, and T. Kitamori, "Transport of a Micro Liquid Plug in a Gas-Phase Flow in a Microchannel," *Micromachines*, vol. 9, no. 9, doi: 10.3390/mi9090423.
- [22] T. Ishida, D. McLaughlin, Y. Tanaka, and T. Omata, "First-come-first-store microfluidic device of droplets using hydrophobic passive microvalves," *Sensors and Actuators B: Chemical*, vol. 254, pp. 1005-1010, 2018/01/01/ 2018, doi: <https://doi.org/10.1016/j.snb.2017.07.154>.
- [23] K. Kobayashi and H. Onoe, "Microfluidic-based flexible reflective multicolor display," *Microsystems & Nanoengineering*, vol. 4, no. 1, p. 17, 2018/07/16 2018, doi: 10.1038/s41378-018-0018-1.
- [24] S. Hao *et al.*, "Progress in adsorptive membranes for separation – A review," *Separation and Purification Technology*, vol. 255, p. 11772, 01/15 2021, doi: 10.1016/j.seppur.2020.117772.
- [25] B. Daelemans *et al.*, "Adsorptive separation using self-assembly on graphite: from nanoscale to bulk processes," *Chemical Science*, 10.1039/D2SC01354A vol. 13, no. 31, pp. 9035-9046, 2022, doi: 10.1039/D2SC01354A.
- [26] M. Pagliai, S. Caporali, M. Muniz-Miranda, G. Pratesi, and V. Schettino, "SERS, XPS, and DFT Study of Adenine Adsorption on Silver and Gold Surfaces," *The*

- Journal of Physical Chemistry Letters*, vol. 3, no. 2, pp. 242-245, 2012/01/19 2012, doi: 10.1021/jz201526v.
- [27] K.-H. Cho, J. Choo, and S.-W. Joo, "Tautomerism of thymine on gold and silver nanoparticle surfaces: surface-enhanced Raman scattering and density functional theory calculation study," *Journal of Molecular Structure*, vol. 738, no. 1, pp. 9-14, 2005/03/14/ 2005, doi: <https://doi.org/10.1016/j.molstruc.2004.11.001>.
- [28] B. Giese and D. McNaughton, "Surface-Enhanced Raman Spectroscopic Study of Uracil. The Influence of the Surface Substrate, Surface Potential, and pH," *The Journal of Physical Chemistry B*, vol. 106, no. 6, pp. 1461-1470, 2002/02/01 2002, doi: 10.1021/jp011986h.
- [29] M. R. Bailey, R. S. Martin, and Z. D. Schultz, "Role of Surface Adsorption in the Surface-Enhanced Raman Scattering and Electrochemical Detection of Neurotransmitters," *The Journal of Physical Chemistry C*, vol. 120, no. 37, pp. 20624-20633, 2016/09/22 2016, doi: 10.1021/acs.jpcc.6b01196.
- [30] K. J. I. Ember *et al.*, "Raman spectroscopy and regenerative medicine: a review," *npj Regenerative Medicine*, vol. 2, no. 1, p. 12, 2017/05/15 2017, doi: 10.1038/s41536-017-0014-3.
- [31] Z. Xu *et al.*, "Topic Review: Application of Raman Spectroscopy Characterization in Micro/Nano-Machining," (in eng), *Micromachines (Basel)*, vol. 9, no. 7, Jul 21 2018, doi: 10.3390/mi9070361.
- [32] S. D. George, "Surface-Enhanced Raman Scattering Substrates: Fabrication, Properties, and Applications," in *Self-standing Substrates: Materials and Applications*, Inamuddin, R. Boddula, and A. M. Asiri Eds. Cham: Springer International Publishing, 2020, pp. 83-118.
- [33] L. Zhang *et al.*, "Liquid/air dynamic behaviors and regulation mechanisms for bioinspired surface," *Applied Physics Reviews*, vol. 9, no. 4, p. 041315, 2022, doi: 10.1063/5.0102883.
- [34] L. Ming, Z. Fusheng, Z. Jianbo, Q. Ji, L. Jing, and S. Wei-Chuan, "Microfluidic surface-enhanced Raman scattering sensor with monolithically integrated nanoporous gold disk arrays for rapid and label-free biomolecular detection," *Journal of Biomedical Optics*, vol. 19, no. 11, p. 111611, 7/1 2014, doi: 10.1117/1.JBO.19.11.111611.
- [35] H.-K. Lee, S.-I. Chang, and E. Yoon, "A Flexible Polymer Tactile Sensor: Fabrication and Modular Expandability for Large Area Deployment," *Microelectromechanical Systems, Journal of*, vol. 15, pp. 1681-1686, 01/01 2007, doi: 10.1109/JMEMS.2006.886021.
- [36] 趙伯宣, "微流道與微流井陣列之表面增強拉曼散射平台結合機器學習以進行抗生素輔助之快速細菌鑑別," 碩士, 生醫電子與資訊學研究所, 國立臺灣大學, 台北市, 2022. [Online]. Available: <https://hdl.handle.net/11296/42gec4>